

1
2
3
4
5
6
7
8
9
10
11
12
13
14
15
16
17
18
19
20
21
22
23
24
25
26

Lipolysis of bone marrow adipocytes is required to fuel bone and the marrow niche during energy deficits

Ziru Li¹, Emily Bowers², Junxiong Zhu^{3,4}, Hui Yu¹, Julie Hardij¹, Devika P. Bagchi¹, Hiroyuki Mori¹, Kenneth T. Lewis¹, Katrina Granger¹, Rebecca L. Schill¹, Steven M. Romanelli¹, Simin Abrishami², Kurt D. Hankenson³, Kanakadurga Singer^{1,2}, Clifford J. Rosen⁵, and Ormond A. MacDougald^{1,6*}

Affiliations:

1. University of Michigan Medical School, Department of Molecular & Integrative Physiology, Ann Arbor, MI
2. University of Michigan Medical School, Department of Pediatrics, Ann Arbor, MI
3. Department of Orthopedic Surgery, University of Michigan Medical School, Ann Arbor, MI
4. Department of Orthopedic Surgery, The Second Affiliated Hospital, Zhejiang University School of Medicine, Hangzhou, China.
5. Maine Medical Center Research Institute, Scarborough, ME
6. University of Michigan Medical School, Department of Internal Medicine, Ann Arbor, MI

***Correspondence to:** Ormond A. MacDougald
NCRC Building 25, Rm. 3686
2800 Plymouth Rd., Ann Arbor, MI 48109
Tel:(734) 647-4880
E-mail: macdougald@umich.edu

27 **Summary**

28 To investigate roles for bone marrow adipocyte (BMAAd) lipolysis in bone homeostasis, we
29 created a BMAAd-specific Cre mouse model in which we knocked out adipose triglyceride lipase
30 (ATGL, *Pnpla2*). BMAAd-*Pnpla2*^{-/-} mice have impaired BMAAd lipolysis, and increased size and
31 number of BMAAds at baseline. Although energy from BMAAd lipid stores is largely dispensable
32 when mice are fed *ad libitum*, BMAAd lipolysis is necessary to maintain myelopoiesis and bone
33 mass under caloric restriction. BMAAd-specific *Pnpla2* deficiency compounds the effects of
34 caloric restriction on loss of trabecular bone, likely due to impaired osteoblast expression of
35 collagen genes and reduced osteoid synthesis. RNA sequencing analysis of bone marrow
36 adipose tissue reveals that caloric restriction induces dramatic elevations in extracellular matrix
37 organization and skeletal development genes, and energy from BMAAd is required for these
38 adaptations. BMAAd-derived energy supply is also required for bone regeneration upon injury,
39 and maintenance of bone mass with cold exposure.

40

41 **Keywords:** bone marrow adipocyte (BMAAd), bone marrow adipose tissue (BMAT), lipolysis,
42 adipose triglyceride lipase (ATGL), caloric restriction (CR), energy supply, hematopoiesis, bone

43

44

45

46 **Introduction**

47 Bone marrow adipocytes (BMAd) are a heterogeneous cell population that form depots
48 of bone marrow adipose tissue (BMAT) distinct from white, brown, and other adipose tissues
49 (Z. Li, Hardij, Bagchi, Scheller, & MacDougald, 2018). Clinical associations generally
50 demonstrate inverse relationships between BMAT and bone mass (Shen et al., 2007), or
51 BMAT and circulating immune cells (Polineni et al., 2020), which may be due to the
52 interactions between cells within the bone marrow niche. In addition to BMAd, the bone
53 marrow niche contains osteoblasts, osteoclasts, hematopoietic cells, stromal/mesenchymal
54 cells, blood vessels, and nerves (Vogler & Murphy, 1988). The relationships between BMAd,
55 bone cells, and hematopoietic cells are influenced by their shared location within bone, an
56 anatomically restricted system, such that expansion of one cell type is by necessity at the
57 expense of others. For example, elevated BMAT is negatively correlated with low bone mass
58 of aging and diabetes, whereas expansion of BMAT is associated with multiple hematopoietic
59 disorders (Z. Li & MacDougald, 2021). Mechanistic links underlying these associations have
60 proven challenging to investigate because they often involve complex intercellular, endocrine,
61 and/or central mechanisms.

62

63 In addition to serving as an energy source, BMAd potentially influence the marrow niche
64 through cell-to-cell contact, release of extracellular vesicles, and secretion of adipokines (e.g
65 adiponectin) and cytokines (e.g. stem cell factor). Removal of these stimuli in mouse models
66 of lipodystrophy, which lack BMAT, results in increased bone mass (Corsa et al., 2021; Zou
67 et al., 2020; Zou et al., 2019). However, use of these models to investigate the direct effects
68 of BMAT depletion is confounded by concurrent loss of white and brown adipose depots,
69 which also regulate bone mass through myriad mechanisms, including secretion of
70 adipokines (Riddle & Clemens, 2017; Zou et al., 2019). Although loss of BMAT in
71 lipodystrophic mice was integral to the original finding that BMAT is a negative regulator of

72 hematopoiesis, positive effects of BMAT on hematopoiesis have also been observed; these
73 differences are attributed to use of distinct animal models and analysis of different skeletal
74 sites (Ambrosi et al., 2017; Naveiras et al., 2009; Zhou et al., 2017). In rodents, there are two
75 readily identifiable BMAd populations: constitutive BMAT (cBMAT) and regulated BMAT
76 (rBMAT) (Scheller et al., 2015). cBMAT typically exists in distal tibia and caudal vertebrae,
77 appears early in life, and has the histological appearance of white adipose tissue. rBMAT is
78 found in proximal tibia and distal femur, and is comprised of single or clustered BMAds
79 interspersed with hematopoietic cells. Whereas cBMAT generally resists change in response
80 to altered physiological states, rBMAT expands with aging, obesity, diabetes, caloric
81 restriction (CR), irradiation, and estrogen deficiency, and is reduced by cold exposure,
82 fasting, β 3-agonist, exercise, and vertical sleeve gastrectomy (Z. Li et al., 2018; Z. Li et al.,
83 2019). These treatments also cause alterations to the skeleton and/or formation of blood
84 cells, some of which may be secondary to effects on BMAds.

85

86 BMAds have long been believed to fuel maintenance of bone and hematopoietic
87 cellularity because of their shared physical location in the marrow niche. However, this
88 hypothesis has not been formally tested because current methods to target BMAds lack
89 penetrance or cause recombination in other cell types, such as white adipocytes, osteoblasts,
90 or bone marrow stromal cells, complicating the interpretation of interactions between BMAds
91 and cells of the marrow niche. To circumvent this problem, we created a BMAd-specific Cre
92 mouse model based on expression patterns of endogenous *Osterix* and *Adipoq*, and
93 investigated roles for BMAds as a local energy source by deleting *ATGL/Pnpla2*, the rate-
94 limiting enzyme of lipolysis. Consistent with *Pnpla2* deficiency in white and brown adipocytes
95 (Ahmadian et al., 2011), BMAd-*Pnpla2*^{-/-} mice have impaired BMAd lipolysis, resulting in
96 hypertrophy and hyperplasia of BMAT. Despite significant increases in bone marrow
97 adiposity, hematopoietic abnormalities of BMAd-*Pnpla2*^{-/-} mice are negligible under basal

98 conditions. However, the recovery of bone marrow myeloid lineages following sublethal
99 irradiation is impaired with CR, and further reduced by BMAd-*Pnpla2* deficiency. Similarly,
100 proliferative capacity of myeloid progenitors is also decreased with CR, and further inhibited
101 in mice lacking BMAd-*Pnpla2*. Whereas alterations in bone parameters were not observed in
102 *ad libitum* fed BMAd-*Pnpla2*^{-/-} mice, bone loss occurred under conditions of elevated energy
103 needs such as bone regeneration or cold exposure, or reduced energy availability such as
104 CR. Reduction of bone mass in CR BMAd-*Pnpla2*^{-/-} mice is likely due to impaired osteoblast
105 functions such as expression of extracellular matrix genes and creation of osteoid. Gene
106 profiling reveals that *Pnpla2* deletion largely blocks CR-induced genes within pathways of
107 extracellular matrix organization and skeletal development, indicating that BMAd-derived
108 energy contributes to skeletal homeostasis under conditions of negative energy balance.

109

110 **Results**

111 **Generation of a BMAd-specific Cre mouse model (BMAd-Cre).** Based on previous
112 studies showing that *Osterix* traces to osteoblasts and BMAds, but not to white adipocytes
113 (Chen & Long, 2013; Mizoguchi et al., 2014), we used CRISPR/Cas9 to create *Osterix-FLPo*
114 mice with an in-frame fusion of *Osterix* and optimized *FLPo*, separated by a *P2A* self-
115 cleaving sequence to allow independent functioning of the two proteins (Figure 1A). To
116 validate tissue-specific expression and FLPo efficiency, we bred *Osterix-FLPo* mice to FLP-
117 dependent EGFP reporter mice, and observed EGFP-positive osteocytes, osteoblasts,
118 BMAds, and a subset of marrow stromal cells within the bone (Figure 1B and 1C).

119

120 We next created FLPo-dependent *Adipoq-Cre* (FAC) mice, which contain an internal
121 ribosome entry sequence (IRES) followed by FLPo-dependent *Cre* in reverse orientation
122 within the 3'-untranslated region (UTR) of endogenous *Adipoq* gene (Figure 1D). FLPo
123 expressed from the *Osterix* locus recombines *Cre* to the correct orientation in progenitors of

124 osteoblasts and BMAd. However, because *Adipoq* is selectively expressed in adipocytes
125 (Eguchi et al., 2011), Cre is expressed in BMAd, but not in osteoblasts or other adipose
126 depots. Consistent with this schema, Cre in the correct orientation (flipped band, Figure 1 -
127 figure supplement 1A-1C) is only observed in caudal vertebral DNA of mice positive for at
128 least one copy each of *Osterix* (Mut band) and FAC (Ori band). The correct insertion of the
129 sequence in *Adipoq* 3'-UTR was validated by Sanger sequencing following genomic PCRs
130 that spanned endogenous *Adipoq* sequences, homology arms, IRES and Cre (Figure 1 -
131 figure supplement 1D). To investigate the cell type-specificity of Cre activity, we next bred
132 *BMAd-Cre* mice to mT/mG reporter mice (Muzumdar, Tasic, Miyamichi, Li, & Luo, 2007)
133 (Figure 1E), in which all tissues and cells express red fluorescence (membrane-targeted
134 tdTomato; mT) at baseline, and will express membrane-targeted EGFP in the presence of
135 cell-specific Cre. We observed loss of tdTomato and gain of EGFP in BMAT depots of caudal
136 vertebrae (tail) and tibiae, but not in brown or white adipose depots, or other tissues/organs
137 such as liver, pancreas, muscle and spleen (Figure 1E and Figure 1 - figure supplement 1E).
138 The correct orientation of Cre (flipped band) was also observed in mRNA isolated from distal
139 tibiae and caudal vertebrae, but not WAT depots, of *Osterix-FLPo* mice positive for FAC
140 (Figure 1 - figure supplement 1F). To evaluate conditions optimal for Cre-induced
141 recombination, we visualized conversion of tdTomato to EGFP in *BMAd-Cre* mice at various
142 ages and with different FAC copy numbers (Figure 1 - figure supplement 1G-1H) and found
143 that the proportion of EGFP-positive BMAd increases with age and number of FAC alleles.
144 Indeed, Cre efficiency is ~80% in both male and female mice over 16 weeks of age with one
145 Cre allele, and over 90% at 12 weeks of age in mice with two Cre alleles.

146

147 Previous studies found that a randomly inserted *Adipoq-Cre* bacterial artificial
148 chromosome (BAC) causes recombination in osteoblasts (Bozec et al., 2013; Eguchi et al.,
149 2011; Mukohira et al., 2019); thus, we tested whether this observation is true in *BMAd-Cre*

150 mice, which rely on endogenous *Adipoq* expression that is restricted by *Osterix*. When
151 *BMAAd-Cre* mice are bred to mT/mG reporter mice, only tdTomato-positive cells are
152 detectable on trabecular bone surfaces (Figure 1F), suggesting that osteoblasts are not
153 targeted. However, labeling of a small subset of stromal/dendritic cells is consistently
154 observed, likely due to expression of *Adipoq* within this cell population (Mukohira et al.,
155 2019).

156

157 Although insertion of the FLPo-activated Cre cassette into the 3'-UTR of endogenous
158 *Adipoq* overcomes potential problems that arise from random genomic integration, we
159 considered the possibility that placement of the IRES-Cre cassette within the 3'-UTR might
160 alter the expression and/or secretion of adiponectin. Although insertion of the IRES-Cre
161 cassette may cause a slight reduction in mRNA expression in whole bone, the adiponectin
162 mRNA in white adipose tissue is elevated by more than 3 fold (Figure 1 - figure supplement
163 2A). Thus, the cassette itself does not limit expression of mRNA. Instead, it appears that the
164 2 kb IRES-Cre cassette within the 3'-UTR impairs translatability of the mRNA since
165 expression of adiponectin protein in BMAT and WAT is decreased by ~50% (Figure 1 - figure
166 supplement 2B and 2C). Circulating adiponectin concentrations appear to be decreased even
167 further (Figure 1 - figure supplement 2D-2F), perhaps suggesting that flux of translated
168 adiponectin protein is impaired through the secretion pathway. Of note, hypoadiponectinemia
169 is associated with insulin resistance (Cook & Semple, 2010; N. Li et al., 2021), with
170 discrepant reports on osteogenesis (Lewis, Edwards, Naylor, & McGettrick, 2021). Thus, we
171 evaluated systemic metabolism in *BMAAd-Cre* mice and found that body weight, glucose
172 tolerance, WAT depot weights, and tibial trabecular and cortical bone variables are
173 unaffected by this degree of hypoadiponectinemia (Figure 1 - figure supplement 2G-2P). To
174 minimize variability between treatments, all mice used in the following studies were positive

175 for both *Osterix-FLPo* and FAC. Gene knockout mice and their controls were determined by
176 the presence or absence of floxed alleles, respectively.

177

178 **Ablation of adipose triglyceride lipase (ATGL, *Pnpla2*) causes BMAT expansion. A**

179 fundamental function of adipocytes is to store excess energy as triacylglycerols and to
180 release non-esterified fatty acids and glycerol during times of negative energy balance. ATGL
181 is the first and rate-limiting enzyme in the lipolytic process; thus, to determine the
182 physiological functions of BMAd lipolysis in bone metabolism and hematopoiesis, we
183 generated BMAd-*Pnpla2*^{-/-} mice, in which the gene encoding ATGL, *Pnpla2*, is specifically
184 knocked out in BMAds. We validated the deletion of ATGL in caudal vertebrae, because
185 cBMAT is abundant in this location. Mutant *Pnpla2* mRNA is observed in caudal vertebrae of
186 BMAd-*Pnpla2* mice, but not in WAT (Figure 2A). Possible sources for the remaining wildtype
187 (WT) *Pnpla2* signal include periosteal WAT, non-adipocyte cells, or perhaps from incomplete
188 deletion of *Pnpla2* in BMAds. Immunofluorescent staining confirms loss of ATGL in proximal
189 tibial rBMAds of BMAd-*Pnpla2*^{-/-} mice (Figure 2B). ATGL protein is reduced substantially in
190 caudal vertebrae, but not in subcutaneous WAT (Figure 2C), which further confirms
191 specificity of BMAd-Cre recombinase for BMAT.

192

193 To quantify effects of *Pnpla2*-deficiency on bone marrow adiposity and cellularity, we
194 used osmium tetroxide, and hematoxylin and eosin staining to evaluate BMAT quantity and
195 cellular details, respectively. We found that BMAT volume is significantly increased in
196 proximal tibiae and throughout the endocortical compartment of BMAd-*Pnpla2*^{-/-} mice,
197 whereas differences in BMAT volume are not observed in distal tibiae, which is almost
198 completely occupied by BMAT in WT mice (Figure 2D-2F). Histological analyses reveal
199 increased BMAd number in proximal tibiae of BMAd-*Pnpla2*^{-/-} mice (Figure 2G and 2H).
200 Depletion of *Pnpla2* also causes BMAd hypertrophy in both proximal and distal tibia, with an

201 increased proportion of BMAd larger than 500 μm^2 observed in proximal tibia, and larger
202 than 1000 μm^2 observed in distal tibia (Figure 2I and 2J). Secretion of basal glycerol and
203 non-esterified fatty acids (NEFA) from *ex vivo* cultured explants of distal tibial BMAT was not
204 different between genotypes. Whereas forskolin treatment greatly increased lipolysis in
205 BMAT explants from control mice, secretion of glycerol and NEFA from BMAd-*Pnpla2*^{-/-}
206 explants remained unchanged from basal rates (Figure 2K and 2L). These results confirm
207 that BMAd of BMAd-*Pnpla2*^{-/-} mice have impaired lipolysis.

208

209 **BMAd lipolysis is required to maintain bone homeostasis in male mice under**
210 **conditions of CR, but not when mice are fed *ad libitum*.** We next evaluated whether loss
211 of BMAd lipolysis in male BMAd-*Pnpla2*^{-/-} mice is sufficient to influence systemic physiology,
212 or function of bone cells within the marrow niche. In mice fed normal chow *ad libitum*, we did
213 not observe differences in body weight, glucose tolerance, or weights of soft tissue, including
214 subcutaneous WAT (sWAT), epididymal WAT (eWAT) and liver (Figure 3 - figure supplement
215 1A-1E), which further confirms the tissue-specificity of our BMAd-knockout model. As
216 observed above, *Pnpla2* deficiency causes expansion of proximal tibial rBMAT (Figure 3 -
217 figure supplement 1F and 1G). Interestingly, when dietary energy is readily available,
218 trabecular bone volume fraction, bone mineral density and trabecular number tend to be
219 lower in BMAd-*Pnpla2*^{-/-} mice, but no significant differences were observed (Figure 3A-3C).
220 These data also indicate that expansion of BMAT is not sufficient to cause bone loss, and
221 that the correlation between elevated fracture risk and expansion of BMAT under a variety of
222 clinical situations is not necessarily a causal relationship.

223

224 Our experiments in *ad libitum* fed mice suggest that energy released from BMAd is
225 dispensable for bone cell functioning when dietary energy is plentiful, which is supported by

226 the comparable concentrations of glycerol and NEFA in circulation and in bone marrow
227 supernatant in BMAd-*Pnpla2*^{+/+} and BMAd-*Pnpla2*^{-/-} mice (Figure 3 - figure supplement 1H
228 and 1I). To determine whether male BMAd-*Pnpla2*^{-/-} mice have impaired bone homeostasis
229 when dietary energy is limited, we next challenged mice with a 30% CR for six weeks. BMAd-
230 *Pnpla2*^{-/-} mice did not have altered body weight, glucose tolerance, or tissue weights
231 comparing with their controls (Figure 3 - figure supplement 1J-1N), suggesting that BMAds
232 are not a critical source of circulating energy under these conditions. Although *ad libitum* fed
233 BMAd-*Pnpla2*^{-/-} mice have increased rBMAT compared to controls (Figure 3 - figure
234 supplement 1F and 1G), CR stimulates rBMAT expansion in control mice such that levels are
235 comparable between genotypes (Figure 3 - figure supplement 1O and 1P). Interestingly,
236 despite this similarity in BMAT volumes, BMAd-*Pnpla2*^{-/-} mice fed CR diet have reduced
237 trabecular bone volume fraction, connective density, and bone mineral density when
238 compared to controls (Figure 3E). This reduction in bone mass is due to decreased
239 trabecular bone number and increased trabecular spacing, without effects on trabecular
240 thickness (Figure 3D-3F). BMAds are a source of NEFA for vicinal osteoblasts (Maridas et
241 al., 2019); thus, the reduction in trabecular bone in CR BMAd-*Pnpla2*^{-/-} mice likely results
242 from impaired osteoblast function due to insufficient energy available in the bone marrow
243 niche. Consistent with this notion, we observed a trend ($P = 0.07$) towards reduced NEFA
244 concentrations in bone marrow supernatant of CR BMAd-*Pnpla2*^{-/-} mice, whilst circulating
245 glycerol and NEFA were not different between genotypes (Figure 3 - figure supplement 1Q
246 and 1R). Of note, changes in cortical bone area and thickness were not observed in BMAd-
247 *Pnpla2*^{-/-} mice with either *ad libitum* or CR diet (Figure 3 - figure supplement 2A-2D), perhaps
248 because cortical bone surfaces are less active.

249

250 To investigate mechanisms underlying trabecular bone loss in CR BMAd-*Pnpla2*^{-/-} mice,
251 we next measured circulating markers of bone cell activity and performed histomorphometry.

252 Osteoblast and osteoclast numbers are not changed by BMAd-*Pnpla2* deficiency under *ad*
253 *libitum* conditions (Figure 3 - figure supplement 2E and 2F). Although circulating markers of
254 bone formation (P1NP) and osteoclast activation (RANK Ligand) are not altered in BMAd-
255 *Pnpla2*^{-/-} mice, markers for bone resorption (CTX-1) and osteoclast activation (TRACP5b) are
256 decreased (Figure 3 - figure supplement 2G-2J). Although with CR, osteoblast numbers are
257 not altered by a deficiency of BMAT lipolysis, the bone formation marker P1NP is decreased
258 (Figure 3G and 3I), suggesting that osteoblast functions are impaired. Osteoclast numbers
259 are increased in CR BMAd-*Pnpla2*^{-/-} mice, but the osteoclast surface per bone surface
260 (Oc.S/BS) is not changed and osteoclast activation marker, TRACP5b, is decreased (Figure
261 3H and 3J), suggesting the osteoclast functions are inhibited. No differences were observed
262 in RANK Ligand and CTX-1 with CR (Figure 3 - figure supplement 2K and 2L). We then
263 visualized and quantified osteoid thickness with Goldner's trichrome staining and observed a
264 trend towards thinner osteoid layers without affecting osteoid surface (Figure 3K and Figure 3
265 - figure supplement 2M), which could be secondary to impaired secretion of collagen matrix
266 by osteoblasts or to enhanced bone mineralization. Further, we injected mice with calcein to
267 label those bone surfaces undergoing active mineralization. Dynamic histomorphometry data
268 suggests that BMAd-*Pnpla2*^{-/-} mice have less bone-forming surface, as indicated by reduced
269 single-labelled surface and mineral surface (Figure 3L). There were no differences in double-
270 labelled bone surface, inter-label width, mineral apposition rate or osteoid maturation time
271 (Figure 3M and Figure 3 - figure supplement 2N), suggesting that bone mineralization is not
272 affected by loss of BMAd lipolysis. Taken together, these data support a model in which
273 reduced trabecular bone in BMAd-*Pnpla2*^{-/-} mice is likely due to impaired ability of osteoblasts
274 to secrete osteoid.

275

276 **BMAd lipolytic deficiency impairs myelopoiesis during regeneration.** A single rBMAd
277 connects to almost 100 hematopoietic cells (Robles et al., 2019), suggesting that BMAds

278 potentially serve as important local energy sources for hematopoiesis. However, when fed *ad*
279 *libitum*, male BMAd-*Pnpla2*^{-/-} mice do not exhibit differences in mature blood cells
280 populations, as assessed by complete blood cell counts (Table 1) and bone marrow flow
281 cytometry for hematopoietic populations (Table 2 and Figure 4 - figure supplement 1A and
282 1B). Although most hematopoietic stem and progenitor cells (HSPCs) do not depend on
283 BMAd lipolysis, reduced numbers of granulocyte-monocyte progenitors (GMP) are observed
284 in marrow of BMAd-*Pnpla2*^{-/-} mice fed *ad libitum* (Table 2). Of note, with CR, reduced
285 numbers of circulating and bone marrow mature neutrophils are observed in BMAd-*Pnpla2*^{-/-}
286 mice, although GMP numbers, which are the progenitor population, are not altered in CR
287 BMAd-*Pnpla2*^{-/-} mice (Tables 1 and 2), perhaps due to impaired maturation of granulocytes.
288 These data suggest that although myeloid cell defects are observed in BMAd-*Pnpla2*^{-/-} mice,
289 other hematopoietic cell populations can metabolically compensate for the lack of BMAd
290 lipolytic products.

291 To investigate further whether hematopoiesis is dependent upon BMAd lipolysis, we
292 administered a sublethal dose of whole-body irradiation, and evaluated hematopoietic cell
293 recovery. Following irradiation, white and red blood cell depletion and recovery were
294 monitored by complete blood cell counts every 2-3 days (Figure 4 - figure supplement 1C-
295 1E). In *ad libitum* fed mice, HSPCs (Figure 4 - figure supplement 1F and 1G) and
296 mature/immature hematopoietic cells (Figure 4A-4H) are not influenced by deficiency of
297 BMAd-lipolysis. However, CR alone decreases bone marrow cellularity (Figure 4A), and
298 HSPC (Figure 4 - figure supplement 1F and 1G) and neutrophil numbers, without affecting
299 monocytes and lymphocytes (Figure 4B-4E). In CR BMAd-*Pnpla2*^{-/-} mice, HSPCs are not
300 altered compared to CR controls, but bone marrow cellularity, monocytes and neutrophils are
301 decreased further. Preneutrophils and immature neutrophils are also reduced by CR, and
302 show additional decline in CR mice lacking BMAd-*Pnpla2* (Figure 4F-4G), but mature
303 neutrophils are only affected by CR (Figure 4H). These reductions in monocytes and

304 neutrophils suggest that BMAd-lipolysis is required for myeloid cell lineage regeneration
305 when energy supply from circulation is limited. CFU assays, which are optimized for the
306 growth of myeloid progenitor cells (CFU-Granulocytes, CFU-Macrophages and CFU-GM),
307 demonstrate fewer granulocyte progenitor colonies (CFU-G) from CR BMAd-*Pnpla2*^{-/-} mice
308 (Figure 4I). The proliferative capacity of macrophage progenitors (CFU-M) is impaired when
309 derived from BMAd-*Pnpla2*^{-/-} mice fed *ad libitum*, or when derived from CR mice of either
310 genotype (Figure 4J). CR marrow produced fewer granulocyte-macrophage progenitors
311 (CFU-GM), which was further reduced when isolated from mice with impaired BMAd-lipolysis
312 (Figure 4K). These data suggest that proliferative and differentiation capacities of cultured
313 myeloid cell progenitors may have been reprogrammed in the marrow niche when their
314 energy supply is restricted either by diet or impaired BMAd lipolysis (Figure 4L).

315

316 **BMAd lipolysis is not required to maintain bone homeostasis under calorie-restricted**
317 **conditions in female mice.** To determine whether sex influences responses of BMAd-

318 *Pnpla2*^{-/-} mice to CR, we performed similar experiments in female mice at 20 weeks of age.
319 As expected, after six weeks of CR, both control and knockout mice exhibited comparable
320 reduced body weights, random blood glucose concentrations, and tissue weights (Figure 3 -
321 figure supplement 3A and 3B). Although CR and *Pnpla2* deficiency cause expansion of
322 proximal tibial rBMAT (Figure 3 - figure supplement 3C), neither CR nor BMAd *Pnpla2*
323 deletion cause alterations in trabecular or cortical bone variables in female mice (Figure 3 -
324 figure supplement 3D and 3E). Consistent with these findings, previous studies showed that
325 CR adult or aged female mice have milder bone loss than in males (Z. Li & MacDougald,
326 2021). Although male BMAd-*Pnpla2*^{-/-} mice exhibited deficiencies in circulating neutrophils,
327 experiments with female mice did not reveal differences in white or red blood cell populations
328 (Figure 3 - figure supplement 3F). We next considered whether estrogen protects female
329 mice from CR-induced osteoporosis. Thus, we ovariectomized control and BMAd-*Pnpla2*^{-/-}

330 mice two weeks prior to initiation of CR. Following initiation of CR, both control and knockout
331 mice demonstrated rapid reduction in body weight for two weeks, then gradually stabilized
332 during the following ten weeks (Figure 3 - figure supplement 4A). We did not observe
333 significant differences in glucose tolerance or bone length with CR or *Pnpla2* deletion (Figure
334 3 - figure supplement 4B and 4C). Additionally, although CR caused reduction in tissue
335 weights, these variables were not different between genotypes (Figure 3 - figure supplement
336 4D). Interestingly, despite the dramatic increases of BAMT responding to CR or BMAAd-
337 *Pnpla2* deficiency, bone volume fraction and trabecular number were increased by CR in
338 ovariectomized mice (Figure 3 - figure supplement 4E and 4F), suggesting that the metabolic
339 benefits of CR diet combat detrimental effects of estrogen deficiency and/or aging. Although
340 we observed a trend toward reduced trabecular thickness in *Pnpla2*-deficient mice, other
341 skeletal parameters were not affected (Figure 3 - figure supplement 4F).

342

343 **Coupling of BMAAd *Pnpla2* deletion and CR results in extensive alterations to the bone**
344 **marrow transcriptome.** To determine mechanisms by which BMAAd *Pnpla2* deficiency
345 causes bone loss in CR male mice, we profiled overall gene expression using bulk RNAseq
346 in bone marrow plugs from distal tibiae, a skeletal location highly enriched with BMAT. PCA
347 plots show that RNA profiles from CR groups are distinct from *ad libitum* controls (Figure 5 -
348 figure supplement 1A). Whereas *Pnpla2* deficiency does not cause gene expression to
349 diverge substantially in mice fed *ad libitum*, loss of *Pnpla2* interacts with CR to cause a well-
350 segregated pattern of gene expression (Figure 5 - figure supplement 1A). By our criteria (padj
351 < 0.05 , $|\log_2 \text{fold change}| > 1$), CR changes expression of 1,027 genes compared to *ad libitum*
352 controls. Although *Pnpla2* deficiency alone only alters 10 genes in BMAAd-*Pnpla2*^{-/-} mice fed
353 *ad libitum*, loss of *Pnpla2* in CR mice causes alterations in 1,060 genes (Figure 5 - figure
354 supplement 1B). Analyses of genes regulated in BMAAd-*Pnpla2*^{+/+} mice with CR reveals four
355 distinct clusters (Figure 5A). Approximately 80% of genes fall in cluster 1, which are

356 upregulated by CR in control mice, with induction largely blocked by *Pnpla2* deficiency in CR
357 mice. Pathway analyses of cluster 1 with Metascape (<https://metascape.org>) reveals that
358 regulated genes are associated with vasculature development and cellular response to
359 growth factor stimulus, which likely reflects adaptation mechanisms to compensate for energy
360 insufficiency (Figure 5 - figure supplement 1C). In addition, genes associated with skeletal
361 system development, extracellular matrix organization, and adipogenesis pathways are
362 upregulated by CR in control mice, but these effects are blunted by *Pnpla2* deletion (Figure 5
363 - figure supplement 1C). Cluster 2 includes genes that are mildly upregulated by CR in
364 control mice and are further increased with *Pnpla2*-deficiency. However, no specific
365 pathways are enriched in this gene set (Figure 5 - figure supplement 1D). Cluster 3 highlights
366 genes that are downregulated by CR treatment regardless of genotype (Figure 5 - figure
367 supplement 1E), and which are associated with B cell proliferation and interleukin-8
368 production, which may partially explain the changes observed in hematopoietic cellularity.
369 Cluster 4 contains 80 genes that are down-regulated independently by CR and *Pnpla2*-
370 deficiency, and are associated with regulation of ossification and calcium-mediated signaling
371 (Figure 5 - figure supplement 1F).

372

373 To evaluate further whether BMAAd-*Pnpla2* is required for the adaptation of BMAT to CR,
374 we graphically ordered genes from those maximally induced to those most repressed by CR
375 in control mice (Figure 5B; red dots). Of these genes, 67.7% do not meet our criteria for
376 regulated expression by CR in BMAAd-*Pnpla2*^{-/-} mice (blue dots). Pathway analyses on the
377 32.3% of genes regulated by CR regardless of *Pnpla2* deficiency reveals association with
378 ribonuclease activity, response to hormones and other transmembrane signaling pathways
379 (Figure 5 - figure supplement 2A). Pathway analyses of genes for which *Pnpla2* is required
380 for response to CR identifies vasculature development and cellular response to growth factor
381 stimulus, similar to cluster 1, followed closely by skeletal system development, adipogenesis

382 genes, and extracellular matrix organization pathways (Figure 5C). A heatmap shows that the
383 adipogenic genes, including *Adipoq*, *Fabp4*, *Cebpa*, *Lipe*, *Lpl*, *Ppar α* , *Ppar γ* , *Scd1*, *Plin1*,
384 *Cd36*, *Fasn* and *Acaca*, are upregulated by CR in control mice (Figure 5D), a subset of which
385 were confirmed by qPCR (Figure 5 - figure supplement 2B). These changes may help explain
386 molecular mechanisms underlying BMAT expansion following CR. It is important to note that
387 whereas CR BMAd-*Pnpla2*^{+/+} and BMAd-*Pnpla2*^{-/-} mice had comparable amounts of BMAT
388 (Figure 3 - figure supplement 1O and 1P), adipocyte gene expression is greatly suppressed
389 in mice with BMAT lacking *Pnpla2* (Figure 5D). This observation is consistent with prior work
390 showing that adipocyte-specific deletion of *Pnpla2* results in decreased expression of genes
391 associated with lipid uptake, synthesis, and adipogenesis (Schoiswohl et al., 2015), perhaps
392 because NEFA and associated metabolites act as PPAR ligands are decreased (Mottillo,
393 Bloch, Leff, & Granneman, 2012). In addition, genes related to endogenous fatty acid
394 biosynthesis are also increased by CR in BMAd-*Pnpla2*^{+/+} mice, but not in mice lacking
395 *Pnpla2* (Figure 5 - figure supplement 2C). Interestingly, myeloid leukocyte differentiation
396 genes follow a similar pattern (Figure 5 - figure supplement 2D), which may contribute to
397 reduced neutrophil production and impaired myeloid cell proliferation of CR BMAd-*Pnpla2*^{-/-}
398 mice (Tables 1 and 2, and Figure 4).

399

400 We previously observed increased bone loss in BMAd-*Pnpla2*^{-/-} mice challenged with CR
401 (Figure 3). To investigate potential mechanisms underlying this bone loss, we analyzed
402 pathways from Cluster 1 related to bone metabolism, skeletal system development and
403 extracellular matrix organization. Interestingly, osteoblast-derived alkaline phosphatase
404 (*Alp*), *Col1a1* and *Col1a2*, and bone marrow Fgf/Fgfr and Wnt signaling-related molecules
405 are highly induced by CR in control mice but not in *Pnpla2*-deficient mice (Figure 5E); many
406 of these genes are also found in the ossification pathway (data not shown). Multiple collagen
407 genes, *Lox*, and *Adamts* (A Disintegrin and Metalloproteinase with Thrombospondin motifs)

408 family members, which are multidomain extracellular protease enzymes and play key roles in
409 extracellular matrix remodeling, are also upregulated by CR in control mice, with effects
410 largely eliminated by *Pnpla2* deficiency (Figure 5F). These findings may partially explain why
411 osteoid thickness tends to be thinner in BMAAd-*Pnpla2*^{-/-} mice (Figure 3K). In this regard, 20
412 collagen genes are significantly up-regulated in control mice following CR (Figure 5 - figure
413 supplement 2E), whereas only four collagen genes are elevated in CR BMAAd-*Pnpla2*^{-/-} mice.
414 Taken together, these data suggest that under conditions of limited dietary energy, BMADs
415 provide energy to maintain osteoblast functions, including the secretion of collagen matrix for
416 osteoid synthesis.

417

418 **BMAAd lipolysis is required for trabecular and cortical bone regeneration.** To test
419 whether BMADs are a critical source of local energy under conditions where energy needs
420 are elevated, we investigated the impact of CR and BMAAd *Pnpla2* deficiency on bone
421 regeneration. To do this, we created a 0.7 mm hole in the proximal tibia, approximately 1 to 2
422 mm distal from the growth plate, and evaluated trabecular and cortical parameters nine days
423 later (Figure 6A). As expected, CR impairs formation of new trabecular bone in the region of
424 interest (ROI) by decreasing trabecular bone volume fraction, bone mineral density, and bone
425 mineral content (Figure 6B). Importantly, these effects of CR are mimicked by BMAAd-specific
426 *Pnpla2* deletion; however, gene deletion does not compound effects of CR on impaired bone
427 regeneration, perhaps because bone volume is already low with either CR or *Pnpla2*
428 deficiency alone. We then visualized newly formed cortical bone with Safranin O/ Fast Green
429 (SO/FG) staining of paraffin-embedded proximal tibia sections (Figure 6C). Of note, both
430 bone marrow stromal and periosteal cells contribute to the cortical bone regeneration and are
431 derived from common mesenchymal progenitors (Duchamp de Lageneste et al., 2018).
432 Although deficiency of BMAAd-lipolysis is unlikely to affect the periosteal cell functions when
433 the cortical bone is intact, it may interact with this cell population during bone regeneration.

434 CR also impaired formation of new cortical bone by decreasing cortical bone volume fraction,
435 bone mineral density, and bone mineral content. As with trabecular bone formation, effects of
436 CR on cortical bone are mimicked by BMAd-specific depletion of *Pnpla2*, but effects of gene
437 deletion do not exacerbate CR-induced impaired bone regeneration (Figure 6D). Taken
438 together, these data provide compelling evidence that under conditions where energy
439 requirements are high, BMAd provide a critical local energy source for bone regeneration.

440

441 **Energy from BMAd protects against bone loss caused by chronic cold exposure.** To
442 explore further under what conditions BMAd lipolysis may be critical for bone cell functions,
443 control and BMAd-*Pnpla2*^{-/-} female mice at 20 weeks of age were housed at room (22°C) or
444 cold (5°C) temperatures for three weeks. Cold exposure is well-documented to increase
445 energy expenditure and adaptive thermogenesis, largely fueled by energy stored in WAT
446 depots. As expected (Scheller et al., 2015; Scheller et al., 2019), cold exposure results in
447 smaller regulated BMAds within the proximal tibia of BMAd-*Pnpla2*^{+/+} mice (Figure 6E and
448 6F). In contrast, BMAd size is increased at baseline in BMAd-*Pnpla2*^{-/-} mice, with no
449 reduction observed with cold exposure (Figure 6E and 6G). These data indicate that intact
450 BMAd lipolysis is required for reduction of BMAd size with cold exposure. We then evaluated
451 bone mass by μ CT and found that whereas trabecular bone of the proximal tibia is
452 maintained in BMAd-*Pnpla2*^{+/+} mice with cold stress, trabecular bone volume fraction and
453 bone mineral density decline with cold exposure in BMAd-*Pnpla2*^{-/-} mice (Figure 6I). These
454 results indicate that lipolysis from vicinal BMAds is required for maintenance of bone when
455 energy needs are high or when energy supply is limited.

456

457 **Discussion**

458 To date, investigation of the physiological functions of BMAT have been hampered by the
459 lack of a BMAd-specific mouse model. Although a number of BMAT depletion models show

460 high bone mass, including A-ZIP (Naveiras et al., 2009), *Adipoq*-driven DTA (Zou et al.,
461 2019), and *Adipoq*-driven loss of *Ppar γ* (Wang, Mullican, DiSpirito, Peed, & Lazar, 2013),
462 *Lmna* (Corsa et al., 2021), or *Bscl2* (McIlroy et al., 2018), these lipodystrophic mice also lack
463 white and brown adipose depots and thus exhibit global metabolic dysfunction, including fatty
464 liver, hyperlipidemia and insulin resistance. Of note, *Adipoq*-driven Cre used in those studies
465 also causes recombination in bone marrow stromal cells (Mukohira et al., 2019). Similarly,
466 mouse models or treatments that result in BMAT expansion, such as *Prx1*-driven *Pth1r*
467 knockout mice (Fan et al., 2017), CR, thiazolidinedione administration, estrogen-deficiency,
468 and irradiation (Z. Li & MacDougald, 2021), also cause bone loss, but again, effects on bone
469 may be secondary to lack of promoter specificity or systemic effects. Lineage tracing studies
470 have previously been performed to determine cell-specific markers for BMAd. For example,
471 both *Prx1* and *Osterix* are restricted to bone and trace to 100% of BMAd, but are also
472 expressed in mesenchymal cells (Logan et al., 2002; Mizoguchi et al., 2014). *Nestin* and
473 leptin receptor (*LepR*) label over 90% of BMAd, but also trace to stromal cells (Zhou et al.,
474 2017). Whereas Pdgf-receptor α (*PdgfR α*)-driven Cre expression causes recombination in all
475 white adipocytes, only 50-70% of BMAd are traced (Horowitz et al., 2017). Thus, our
476 strategy for targeting BMAd using dual expression of *Osterix* and *Adipoq* will be critical for
477 improving interpretability of experiments on roles for BMAd in the marrow niche.

478

479 After generating this novel BMAd-specific Cre mouse model, we successfully ablated
480 *Pnpla2* in BMAd, and demonstrated the necessity of ATGL in BMAd lipolysis. Our studies
481 directly demonstrate for the first time the importance of BMAd lipolysis in myelopoiesis and
482 bone homeostasis under conditions of energetic stress, including CR, irradiation, bone
483 regeneration and cold exposure. With the loss of peripheral WAT in CR mice, there is a
484 dramatic increase in BMAT throughout the tibia, and this is accompanied by increased
485 expression of adipocyte genes, including those involved in lipid uptake, de novo lipogenesis,

486 and lipolysis. BMAT expansion with CR has been observed in both rodents and humans
487 (Cawthorn et al., 2014; Devlin et al., 2010; Fazeli et al., 2021), and mechanisms underlying
488 this observation are still not fully understood. We speculate that CR promotes lipolysis in
489 peripheral adipose tissues, and the released non-esterified fatty acids have increased flux to
490 bone marrow, where they are used either directly to maintain hematopoiesis and bone
491 homeostasis, or used indirectly after having been stored and released from BMAT. Thus, we
492 speculate that BMAd have elevated rates of lipid uptake, lipogenesis and lipolysis with CR.
493 However, when BMAd lipolysis is impaired, this dynamic cycle is halted, which is reflected by
494 the blunted induction of adipocyte genes in response to CR. This BMAd quiescence causes a
495 shortfall in local energy supply and contributes to hematopoietic cell and osteoblast
496 dysfunction. In this regard, two major collagens secreted by osteoblasts, *Col1a1* and *Col1a2*,
497 and *Alpl* were increased by CR in WT mice, but not in calorie-restricted BMAd-*Pnpla2*^{-/-} mice.
498 These data are consistent with the trend for thinner osteoid observed in CR BMAd-*Pnpla2*^{-/-}
499 mice and reduced circulating concentrations of the bone formation marker P1NP. Although
500 bone mineralization is not impaired, new bone forming surface is reduced in CR mice that
501 lack BMAd lipolysis. In addition, the number of osteoclasts on trabecular bone surface is
502 higher in CR BMAd-*Pnpla2*^{-/-} mice; however, osteoclast surface per bone surface and a
503 circulating marker of bone turnover (CTX-1) are not increased. A serum marker for osteoclast
504 activity, TRACP5b, is decreased in BMAd-*Pnpla2*^{-/-} mice either fed *ad libitum* or a CR diet.
505 Taken together, our studies suggest that bone mass reduction in CR BMAd-*Pnpla2*^{-/-} mice is
506 less likely due to degradation of bone by osteoclasts, and more likely due to impaired
507 osteoblast function, including osteoid production.

508

509 Interestingly, the contributions of BMAd lipolysis to bone homeostasis appear to be more
510 important in male mice compared to females. Although we considered that a stronger
511 phenotype might be revealed in female mice following estrogen depletion, the low bone mass

512 observed with ovariectomy or CR may represent a critical threshold that is strongly defended
513 through mechanisms independent of BMAd lipolysis. Alternatively, it is possible that
514 androgens increase energy requirements of bone such that male mice are more dependent
515 on BMAd lipolysis under stressful conditions. Importantly, we observed that bone volume
516 fraction and trabecular number were increased by 12 weeks of CR in OVX mice of both
517 genotypes, suggesting that the metabolic and anti-aging benefits of CR somehow block the
518 bone loss associated with estrogen deficiency as mice age to 40 weeks.

519 Surprisingly, despite expansion of BMAT in *ad libitum*-fed BMAd-*Pnpla2*^{-/-} male and
520 female mice, we did not observe differences in skeletal parameters. Indeed, the critical role of
521 BMAd lipolysis in fueling osteoblast was observed in BMAd-*Pnpla2*^{-/-} male mice only when
522 energy needs were high, or the availability of dietary energy was low. Of note, cellular protein
523 synthesis typically uses 25 to 30% of the oxygen consumption coupled to ATP synthesis
524 (Rolfe & Brown, 1997), and this percentage may be higher in osteoblasts since protein
525 synthesis and translation are integral to cell function. Additionally, fatty acids contribute
526 substantially to the energy demands of bone tissue and cells (Adamek, Felix, Guenther, &
527 Fleisch, 1987), and in the absence of BMAd lipolysis, these energy needs must be met from
528 circulating lipids, glucose, lactate and amino acids. Uptake of fatty acids by osteoblasts is
529 likely mediated by the CD36 fatty acid translocase, which is required in mice to maintain
530 osteoblast numbers and activity (Kevorkova et al., 2013). Further, impairment of fatty acid
531 oxidation in osteoblasts and osteocytes led to reduced postnatal bone acquisition in female,
532 but not male mice. Interestingly, significant increases in the osteoid thickness, osteoid
533 volume per bone volume, and the osteoid maturation time suggest that a mineralization
534 defect occurs in mice unable to oxidize fatty acids obtained not only from BMAds, but also
535 from circulation (Kim et al., 2017).

536 Given extensive literature describing interactions between BMAd and hematopoietic
537 cells (Lee, Al-Sharea, Dragoljevic, & Murphy, 2018; Valet et al., 2020), we were surprised at
538 the lack of substantial changes in hematopoietic progenitors, white blood cells, and red blood
539 cells in BMAd-*Pnpla2*^{-/-} mice under basal and CR conditions. One possibility is that skeletal
540 sites containing low BMAd numbers, including vertebrae, sternum, ribs and pelvis, may allow
541 compensatory formation of circulating mature blood cells (Kricun, 1985). In addition,
542 hematopoietic progenitors and mature blood cell populations were not substantially altered in
543 bone marrow of long bones, with the exception of myeloid differentiation into neutrophils,
544 suggesting that hematopoietic cellularity is generally maintained despite expansion of BMAT
545 volume. Although hematopoietic progenitors and mature cells can use lipids for energy,
546 glucose serve as the major source of energy for glycolysis and oxidative metabolism in these
547 cell populations (Jeon, Hong, Kim, & Lee, 2020; Roy, Biswas, Verfaillie, & Khurana, 2018). It
548 is perhaps unsurprising, given the importance of blood cell production in maintaining life, that
549 there is a great deal of metabolic flexibility when it comes to fuel sources for hematopoiesis.
550 While HSPC numbers are unaltered in our BMAd-*Pnpla2*^{-/-} mice, myeloid lineage cell
551 recovery is significantly blunted by CR and deficiency of BMAd-lipolysis following sublethal
552 irradiation and in *in vitro* myeloid CFU assays. Myeloid progenitors from CR BMAd-*Pnpla2*^{-/-}
553 mice had an impaired capacity to expand, suggesting that progenitors were reprogrammed in
554 response to energy deficiency in the bone marrow niche. We did not profile the metabolic
555 changes of HSPCs in CR BMAd-*Pnpla2*^{-/-} mice, but it has been reported that fatty acid
556 oxidation is required for HSC asymmetric division to retain the stem cell properties (Ito et al.,
557 2012).

558

559 In summary, we have developed a novel mouse model to specifically evaluate the
560 importance of BMAd as a local energy source. We report that BMAd is a local energy
561 source that support myeloid cell lineage regeneration following irradiation, and maintain

562 progenitor differentiation capacity when systemic energy is limiting. In addition, we find that
563 BMAT serves a highly specialized function to maintain bone mass and osteoblast function in
564 times of elevated local energy needs such as with bone regeneration, increased whole body
565 energy needs from cold exposure, or when dietary energy is limited due to CR.

566

567 **Limitations of Study**

568 There are some limitations to the BMA^d-Cre mice that should be noted. For instance,
569 expression of Cre from the IRES within the 3'-UTR of *Adipoq* is relatively low, and thus rates
570 of recombination are less frequent in young mice than optimal. Mice that are older than 16
571 weeks are suggested for future usage of this Cre mouse model. However, bone formation
572 and turnover rates decrease with age both in mice and humans (Fatayerji & Eastell, 1999;
573 Ferguson, Ayers, Bateman, & Simske, 2003), which may provide challenges for mechanistic
574 studies. The IRES-Cre cassette also causes hypoadiponectinemia so experimental design
575 must include appropriate controls with BMA^d-Cre positive mice with or without floxed genes.
576 Although a total absence of adiponectin reduces bone mass (Naot et al., 2016; Yang et al.,
577 2019), mice with hypoadiponectinemia described here did not exhibit metabolic or bone
578 phenotypes. In retrospect, a better approach might have been to accept loss of one *Adipoq*
579 allele and insert the FAC cassette at the start site of the adiponectin coding region to promote
580 high levels of Cre expression. This strategy might also have allowed inducible knockout of
581 BMA^d genes with tamoxifen through expression of CreERT2, which we found to be too
582 inefficient to be functional when inserted into the 3'-UTR of *Adipoq*, with only 5 to 8% BMA^ds
583 labeled in tamoxifen-treated adult mice. Of note, all mice used in these studies were on a
584 mixed SJL and C57BL/6J background, and mouse strain influences bone mass, and
585 responsiveness of bone to stressors.

586

587 **Materials and Methods**

588 **KEY RESOURCES TABLE**

REAGENT or RESOURCE	SOURCE	IDENTIFIER
Antibodies		
Rabbit monoclonal anti-adiponectin	Sigma-Aldrich	A6354
Mouse/Rat FABP4/A-FABP Antibody	R&D Systems	AF1443
alpha Tubulin Monoclonal Antibody	Thermo Fisher Scientific	MA180017
Anti-ERK 2 Antibody (D-2)	Santa Cruz Biotechnology	sc-1647
Anti-Albumin antibody	Abcam	Ab207327
ATGL Antibody	Cell Signaling Technology	2138S
ATGL Antibody	Abcam	ab207799
Anti-GFP antibody	Abcam	ab13970
RFP Antibody Pre-adsorbed	Rockland	600-401-379
Goat anti Rabbit IgG (H+L) Secondary Antibody, Alexa Fluor 594	Invitrogen	A11012
Alexa Fluor 488 goat anti-chicken IgG (H+L)	Invitrogen	A11039
Ly6G FITC	BD Biosciences	551460
CD11b APC	Invitrogen	17-0112-82
CD115 APC-Cy7	Biolegend	135531
CD3e PE-Cy7	Biolegend	100319
CD19 Pacific Blue	Invitrogen	48-0193-82
CD45 AlexaFluor700	BD Biosciences	560510
Gr-1 Biotin	Biolegend	79750
CD11b Biotin	Biolegend	79749
B220 Biotin	Biolegend	79752
CD3e Biotin	Biolegend	79751
TER119 Biotin	Biolegend	79748

Sca1 PE-Cy7	Invitrogen	25-5981-82
cKit (CD117) APC-Cy7	Biolegend	105826
CD150 BrilliantViolet 421	Biolegend	115925
CD48 FITC	Invitrogen	11-0481-85
CD16/32 PerCP-Cy5.5	Biolegend	101324
CD105 APC	Biolegend	120413
CXCR2 PE	Biolegend	149304
CXCR4 PE-Dazzle	Biolegend	146514
CD62L BrilliantViolet 421	Biolegend	104435
Streptavidin BrilliantViolet 510	Biolegend	405233
Chemicals, peptides, and recombinant proteins		
Calcein	Sigma-Aldrich	C0875
EDTA	DOT Scientific Inc	dse57020
Tetroxide Osmium	Electron Microscopy Sciences	19190
Forskolin	Cayman Chemical Company	11018
Bovine Serum Albumin (BSA), Fraction V	Gold Biotechnology	A-421-250
qPCRBio SyGreen Mix Hi-ROX Blue	Innovative Solutions	4SPB20.16
PCRBio HS Taq Mix Red	Innovative Solutions	4SPB10.23
Agarose	Thermo Fisher Scientific	BP160-500
RNA STAT-60	AMSBIO	CS-502
M-MLV Reverse Transcriptase	Thermo Fisher Scientific	28025013
100 bp DNA Ladder	NEB	N3231S
Critical commercial assays		
Acid Phosphatase Leukocyte (TRAP) Kit	Sigma-Aldrich	387A-1KT
Free Glycerol Determination Kit	Sigma-Aldrich	FG0100
NEFA Reagent (NEFA-HR(2))	FUJIFILM Wako Diagnostics	NC9517309
BCA Protein Assay Kit	Thermo Fisher Scientific	23225

RAT/MOUSE P1NP ELISA KIT	Immunodiagnostic Systems Inc	NC9666468
Mouse TRANCE/RANK L/TNFSF11 Quantikine ELISA Kit	R&D Systems	MTR00
MOUSE TRAP ASSAY	Immunodiagnostic Systems Inc	NC9360739
MethoCult™ GF M3534	ATEMCELL	03534
DNA-free™ Kit	Life Technologies	AM1906
Deposited data		
RNA-seq	This study	GSE183784
Experimental models: Organisms/strains		
Mouse: <i>Osterix-FLPo</i>	Generated in University of Michigan Transgenic Animal Model Core	N/A
Mouse: <i>FLPo</i> -dependent <i>Adipoq-Cre</i> (FAC)	Generated in University of Michigan Transgenic Animal Model Core	N/A
Mouse: Frt-floxed EGFP	Generated in University of Michigan Transgenic Animal Model Core	N/A
Mouse: mT/mG	Jackson Laboratory	Stock No. 007676
Mouse: <i>Pnpla2</i> ^{fllox/fllox}	Jackson Laboratory	Stock No. 024278
Oligonucleotides		
Primers for genotyping PCR and qPCR	See Table 3	N/A
Software and algorithms		
Microsoft Office	Microsoft	https://its.umich.edu/communication/collaboration/microsoft-office-365/getting-started

Adobe photoshop	Adobe	https://www.adobe.com/creativecloud/desktop-app.html
Prism 9	GraphPad software	https://www.graphpad.com/
Image J	Image J	https://imagej.nih.gov/ij/
MetaMorph	BioVision Technologies	https://www.biovis.com/metamorph.html
Scano μ CT 100	SCANCO Medical AG	https://www.scanco.ch/
BIOQUANT OSTEO	BIOQUANT Image analysis corporation	https://bioquant.com/
STAR	PMID 23104886	https://github.com/alxexdubin/STAR
DESeq2	PMID 25516281	https://bioconductor.org/packages/release/bioc/html/DESeq2.html
QualiMap-2	PMID 26428292	https://qualimap.comesalab.org
R	The R Foundation	https://www.r-project.org/
Metascape	PMID 30944313	https://metascape.org/gp/index.html

Dragonfly	ORS - OBJECT RESEARCH SYSTEMS	https://www.theobjectsystems.com/dragonfly/index.html
FlowJo	BD Biosciences	https://www.flowjo.com/solutions/flowjo
Other		
Element HT5 Veterinary Hematology Analyzer	Heska	https://www.heska.com/product/element-ht5/
FACSAria III cell sorter	BD Biosciences	N/A
LSRFortessa Cell Analyzer	BD Biosciences	N/A
Nikon A1 Confocal Microscope	Nikon	N/A
Bayer Contour Next Test Glucose Strips	Diabetic Corner	ByrContournext
Scanco μ CT 100 micro-computed tomography system	SCANCO Medical AG	https://www.scanco.ch/
Olympus BX51	Olympus	N/A
StepOnePlus™ Real-Time PCR System	Thermo Fisher Scientific	4376600
Microtome	Leica	RM2235
Cryostat	Leica	N/A
Slide scanner	Nikon	N/A

589

590 **Resource Availability**

591 **Lead contact**

592 Further information and requests for resources and reagents should be directed to and will be fulfilled

593 by the Lead Contact, Ormond A. MacDougald (macdougald@umich.edu).

594

595 **Materials availability**

596 Our *Osterix-FLPo* and FLPo-dependent *Adipoq-Cre* (FAC) mouse models will be available to
597 investigators upon request. All the other data and materials that support the findings of this study are
598 available within the article and supplemental information, or available from the authors upon request.
599

600 **Data availability**

601 The accession number for the BMAT bulk RNA seq data reported in this paper is GEO: GSE183784.

602 This paper does not report original code.

603 **Animal**

604 Generation of BMAAd-specific Cre mouse model. To create a BMAAd-specific Cre mouse
605 model, we expressed mouse codon-optimized FLP (FLPo) (Raymond & Soriano, 2007) from
606 the *Osterix* (*Sp7*) locus to recombine and activate a Cre expressed from the *Adipoq* locus.
607 After designing sgRNA target sequences against 3'-UTR of endogenous *Osterix* (sgRNA:
608 gatctgagctgggtagaggaagg) and *Adipoq* (sgRNA1: tgaacaagtgagtacacgtgtgg; sgRNA2:
609 cagtgagcagaaaaatagcatgg) genes with the prediction algorithm available at
610 <http://crispor.tefor.net>, we cloned sgRNA sequences into an expression plasmid bearing both
611 sgRNA scaffold backbone (BB) and Cas9, pSpCas9(BB) (Ran et al., 2013), which is also
612 known as pX330 (Addgene plasmid ID: 42230; Watertown, MA). Modified pX330 plasmids
613 were injected into fertilized ova. After culture to the blastocyst stage, Cas9 activity was
614 confirmed by sequencing the predicted cut site. We then inserted a DNA fragment containing
615 an in-frame fusion protein between endogenous *Osterix* and FLPo, separated by coding
616 sequence for P2A (porcine teschoviral-1) self-cleavage site to allow the full-length proteins to
617 function independently. We also inserted into the 3'-UTR of *Adipoq* an IRES-F3-Frt-reversed
618 Cre-F3-Frt cassette with ~1kb of 5' and 3' flanking homology-arm sequence. The targeting
619 vectors (Cas9 expression plasmid: 5 ng/ul; donor DNA: 10 ng/ul) were injected into fertilized
620 mouse eggs, which were transferred into pseudopregnant recipients to obtain pups. Tail DNA
621 was obtained for genomic PCR and Sanger sequencing to screen F0 founders for desired
622 genetic modifications at the expected locations. These F0 generation chimeric mice were
623 mated with normal mice to obtain mice that are derived exclusively from the modified
624 fertilized eggs. Germline transmitted mice (F1 generation) carrying the designated genetic
625 modifications were bred with reporter mice to validate the activity and efficiency of FLPo and
626 Cre recombinase. These mice were generated by University of Michigan Transgenic Animal
627 Model Core and MDRC Molecular Genetics Core.
628

629 Validation of Osterix-FLPo specificity and efficiency. Osterix-FLPo mice were bred with FLP-
630 dependent EGFP reporter mice (derived from <https://www.jax.org/strain/012429>; Bar Harbor,
631 ME), provided by Dr. David Olson from the University of Michigan MDRC Molecular Genetics
632 Core. Fresh tissue confocal was performed to validate EGFP expression.

633

634 Validation of the specificity and efficiency of FLPo-activated Adipoq-Cre (FAC) mice. Among
635 80 F0 generation pups, 13 mice carried the FAC cassette. These founder mice were bred
636 with Osterix-FLPo mice and mT/mG reporter mice (Stock No. 007676, Jackson Laboratory;
637 Bar Harbor, ME) to further validate Cre recombinase activity and specificity via fresh tissue
638 confocal and immunofluorescent histology. Every single mouse in F1 generation was
639 confirmed and separated for future breeding. We finally selected F0-#693 → F1-#4376 for
640 BMAd-specific knockout lines. Of note, Osterix-FLPo and FAC mice were generated on a
641 mixed SJL and C57BL/6J background. *Pnpla2*^{flox/flox} mice purchased from Jackson laboratory
642 (Stock No. 024278; Bar Harbor, ME) were on a C57BL/6J background.

643

644 Animal housing

645 Mice were housed in a 12 h light/dark cycle in the Unit for Laboratory Animal Medicine at the
646 University of Michigan, with free access to water. Mice were fed *ad libitum* or underwent
647 caloric restriction, as indicated. All procedures were approved by the University of Michigan
648 Committee on the Use and Care of Animals with the protocol number as PRO00009687.

649

650 Animal Procedures

651 1) 30% CR. After acclimation to single-housing for 2 weeks, and control diet
652 (D17110202; Research Diets; New Brunswick, NJ) for a week, daily food intake was
653 measured for another week. Mice were then fed a 30% CR diet (D19051601; Research
654 Diets; New Brunswick, NJ) daily at ~6 pm, prior to onset of the dark cycle.

655 2) Ovariectomy. Female mice at 16 weeks of age underwent ovariectomy (OVX). After 2
656 weeks recovery, they were either fed an *ad libitum* or 30% CR diet for 12 weeks.

657 3) Proximal tibial defect. Surgeries were performed under isoflurane anesthesia, and
658 subcutaneous 0.1 mg/kg buprenorphine was given in 12-h intervals for peri-/post-operative
659 pain management. The proximal tibial defects were obtained by drilling a hole through
660 anterior cortical and trabecular bone, 1 to 2 mm below the epiphyseal growth plate, with a 0.7
661 mm low-speed drill.

662 4) Cold exposure. Mice were single-housed without nesting materials in thermal
663 chambers for 3 weeks at 5°C.

664 5) Glucose Tolerance Test (GTT). Mice were fasted overnight (16-18 hours). Body
665 weight and fasting glucose levels were measured, followed by an intraperitoneal (i.p.)
666 injection of glucose (1g glucose/kg body weight). Blood glucose was measured with Bayer
667 Contour test strips at 15, 30, 60, 90 and 120 min time points by cutting the tip of tails.

668 6) Whole body irradiation. Irradiations were carried out using a Kimtron IC320 (Kimtron
669 Medical; Oxford, CT) at a dose rate of ~4 Gy/minute with total dosage of 6 Gy in the
670 University of Michigan Rogel Cancer Center Experimental Irradiation Shared Resource.
671 Dosimetry was carried out using an ionization chamber connected to an electrometer system
672 that is directly traceable to a National Institute of Standards and Technology calibration.

673

674 **Fresh tissue confocal microscopy.** *Osterix*-driven EGFP expression and BMA^d-Cre-driven
675 mT/mG reporter mice were sacrificed. Fresh tissues were collected immediately and put in
676 ice-cold PBS, which was protected from light. Soft tissues including adipose tissues and liver
677 were cut into small pieces and placed in a chamber for confocal imaging (Nikon Ti-E Inverted
678 Microscope; Minato City, Tokyo, Japan). Bones were bisected, and butterflied on a coverslip
679 for imaging. Both white field and fluorescent images were taken under 200x magnification.

680

681 **Histology and histomorphometry.** Tissue histology was performed essentially as described
682 previously (Z. Li et al., 2019). Briefly, soft tissues were fixed in formalin, and embedded in
683 paraffin for sectioning. Tibiae were fixed in paraformaldehyde, decalcified in EDTA for at least
684 2 weeks, and followed by post-decalcification fixation with 4% paraformaldehyde. Bone
685 tissues were then embedded in paraffin, sectioned. After staining with hematoxylin and eosin
686 (H&E), soft tissues were imaged with an Olympus BX51 microscope. Bones were stained
687 with H&E or Tartrate-Resistant Acid Phosphatase (TRAP; Sigma-Aldrich, MO) as indicated,
688 and slides were scanned at 200X magnification. Static measurements include bone volume
689 fraction, trabecular bone microstructure parameters, osteoblast number and surface, and
690 osteoclast number and eroded surface. Undecalcified tibia was used for plastic sectioning.
691 Mineralized trabecular bone and osteoid were evaluated with Goldner's Trichrome Staining.
692 For dynamic studies, calcein (C0857; Sigma-Aldrich, MO) dissolved in 0.02 g/ml sodium
693 bicarbonate with 0.9% saline at 20 mg/kg was injected intraperitoneally nine- and two-days
694 before sacrifice for quantification of mineral surface (MS), inter-label width (Ir. L. Wi), and
695 mineral apposition rate (MAR) in tibia. Calculations were made with Bioquant Osteo 2014
696 (Nashville, TN) software in a blinded manner (Merceron et al., 2014; Morse et al., 2014).

697

698 **μ CT analysis.** Tibiae were placed in a 19 mm diameter specimen holder and scanned over
699 the entire length of the tibiae using a μ CT system (μ CT100 Scanco Medical, Bassersdorf,
700 Switzerland). Scan settings were: voxel size 12 μ m, 70 kVp, 114 μ A, 0.5 mm AL filter, and
701 integration time 500 ms. Density measurements were calibrated to the manufacturer's
702 hydroxyapatite phantom. Analysis was performed using the manufacturer's evaluation
703 software with a threshold of 180 for trabecular bone and 280 for cortical bone.

704

705 **Marrow fat quantification by osmium tetroxide staining and μ CT.** After analyses of bone
706 variables, mouse tibiae were decalcified for osmium tetroxide staining, using our previously
707 published method (Scheller et al., 2015). In addition, a lower threshold (300 grey-scale units)
708 was used for proximal tibial rBMAT quantification because density of osmium staining is low
709 due to smaller adipocyte size, and with threshold as 400 grey-scale units for cBMAT in distal
710 tibia.

711

712 **Immunofluorescent staining.** Decalcified tibiae were embedded in OCT compound and
713 used for frozen sectioning at 15 μ m. Excess OCT was removed, and tibial tissues were
714 blocked with 10% goat serum for one hour at room temperature. Primary antibodies for GFP
715 (1:500) and RFP (1:200; Figure 1F) or ATGL (1:100; Figure 2B) were then added to slides
716 and incubated with bone tissues overnight at 4°C. Secondary antibodies (goat anti Rabbit
717 IgG, Alexa Fluor 594 & goat anti-chicken IgG Alexa Fluor 488 or donkey anti rabbit IgG
718 (H+L), Alexa Fluor 488) were added to slides following three washes. Two hours later, DAPI
719 staining was performed. Slides were mounted with prolong gold antifade reagent and
720 imaged.

721 **RNA extraction and quantitative real-time PCR (qPCR).** RNA was extracted from tissues
722 after powdering in liquid nitrogen and lysis in RNeasyStat60 reagent in a pre-cooled dounce
723 homogenizer. Quantitative PCR was performed using an Applied Biosystems QuantStudio 3
724 qPCR machine (Waltham, MA). Gene expression was calculated based on a cDNA standard
725 curve within each plate and normalized to expression of the geometric mean of
726 housekeeping genes *Hprt*, *Rpl32A* and *Tbp*.

727 **Immunoblot.** Detection of proteins by immunoblot was as described previously (Mori et al.,
728 2021).

729 **Ex vivo lipolysis.** Distal tibial BMAT plugs were flushed out from the bone, and four plugs
730 were pooled into one well of a 96-well plate for each n. Pre-warmed 2% BSA HBSS was
731 added to BMAT explants with vehicle (DMSO) or forskolin (FSK, 5 μ M), to activate lipolysis
732 (Litosch, Hudson, Mills, Li, & Fain, 1982). Cultured media was collected hourly for 4 hours,
733 and glycerol and NEFA concentrations were measured with commercially available kits as
734 listed above in reagents.

735

736 **CFU assay.** Bone marrow cells of BMAd-*Pnpla2*^{+/+} and BMAd-*Pnpla2*^{-/-} mice were obtained
737 from femur and tibia. To isolate bone marrow, the bones were flushed with IMDM (Gibco
738 12440; Waltham, MA) containing penicillin-streptomycin antibiotic (Gibco 15270-063;
739 Waltham, MA). Pelleted cells were counted with a hemocytometer, 1X10⁴ cells were plated in
740 Methocult medium (Stem cell M3534; Vancouver, Canada) in 35 mm culture dishes, and cells
741 were then incubated at 37°C in 5% CO₂ with \geq 95% humidity for seven days. CFU-G, CFU-M
742 and CFU-GM colonies on each plate were counted using a microscope with a 4X objective
743 lense.

744

745 **Bulk RNA sequencing.** Distal tibial plugs (cBMAT) from two animals were pooled together
746 for each bulk RNAseq sample. Total RNA was isolated from BMAT for strand specific mRNA
747 sequencing (Beijing Genomics Institute, China). Over twenty million reads were obtained
748 using a paired-end 100 bp module on DNBSEQ platform. The quality of the raw reads data
749 was checked using FastQC (v.0.11.9) and the filtered reads were aligned to reference
750 genome (UCSC mm10) using STAR with default parameters. All samples passed the post-
751 alignment quality check (QualiMap (v.2.2.1). The DEseq2 method was used for differential
752 expression analysis with genotype (*Pnpla2*^{+/+} vs. *Pnpla2*^{-/-}) and treatment (CR vs. *ad libitum*)
753 as the main effects. Gene ontology analysis was done using MetaScape. The Principal

754 Component Analysis (PCA) plot was generated using the PlotPCA function building in
755 DESeq2 package. To compare the number of differentially expressed genes between
756 genotype/treatment groups, volcano plots were constructed using the Enhanced Volcano
757 package under R environment. Heatmap plots were generated using pheatmap package
758 under R environment and the complete-linkage clustering method was used for the
759 hierarchical cluster of genes. These data are available through NCBI GEO with the following
760 accession number, GSE183784.

761

762 **Flow cytometry.** Femurs were isolated from mice. Bone marrow was harvested by flushing
763 the femurs with 1 mL of ice-cold PEB (1X PBS with 2 mM EDTA and 0.5% bovine serum
764 albumin). Red blood cells were lysed once by adding 1 mL of RBC Lysis Buffer (155 mM
765 NH_4Cl , 10 mM KHCO_3 , 0.1 mM EDTA) and gently pipetting to mix. Cells were immediately
766 pelleted by centrifugation and resuspended in 1 mL of ice-cold PEB. Cells were stained for
767 30 minutes in PEB buffer with the indicated antibodies below and analyzed on the BD
768 LSRFortessa or BD FACSAria III. Data was analyzed using FlowJo software (BD
769 Biosciences, version 10.8). Dead cells and doublets were excluded based on FSC and SSC
770 distribution. To stain for mature leukocytes antibodies used were against CD45, Ly6G,
771 CD11b, CD115, CD19, and CD3e. All CD45⁺ cells were gated first for further identification.
772 Neutrophils were defined as Ly6G⁺CD11b⁺, monocytes were defined as Ly6G⁻
773 CD11b⁺CD115⁺, B cells were defined as Ly6G⁻CD11b⁻CD19⁺, and T cells were defined as
774 Ly6G⁻CD11b⁻CD3e⁺. To stain for bone marrow neutrophil populations, antibodies used were
775 against Ly6G, CD11b, cKit, CXCR2, CXCR4, and CD62L. Pre-neutrophils were defined as
776 Ly6G⁺CD11b⁺cKit⁺, immature neutrophils were defined as Ly6G⁺CD11b⁺cKit⁻CXCR2^{lo}, and
777 mature neutrophils were defined as Ly6G⁺CD11b⁺cKit⁻CXCR2^{hi}. To stain for hematopoietic
778 stem and progenitor cells (HSPCs) antibodies used were against a lineage panel (Gr-1,
779 CD11b, B220, CD3e, TER119), cKit, Sca-1, CD150, CD48, CD105, and CD16/32. After

780 gating on the lineage⁻ population, HSPCs were defined as follows; HSCs as
781 LSKCD150⁺CD48⁻, MPPs as LSKCD150⁻CD48⁻, HPC1 as LSKCD150⁻CD48⁺, HPC2 as
782 LSKCD150⁺CD48⁺, GMPs as LKCD150⁻CD16/32⁺, PreGMs as LKCD150⁻CD105⁻, PreMegEs
783 as LKCD150⁺CD105⁻, and PreCFUe as LKCD150⁺CD105⁺. LSK = lineage⁻Sca1⁺cKit⁺, LK =
784 lineage⁻cKit⁺.

785

786 **Bone regeneration analysis.** Nine days after the proximal tibial defect surgery, proximal
787 tibiae were collected for μ CT scanning. After construction, new generated trabecular and
788 cortical bone were quantified by Dragonfly software (Montréal, Canada). Under the full view
789 of 3D and 2D images, a cylinder-shaped region of interest (ROI) was defined in trabecular or
790 cortical bone defect area (as shown in Figure 5A) with 3D dimension as 0.3 mm (diameter) x
791 0.7 mm (height) for trabecular bone and 0.3 mm (diameter) x 0.2 mm (height) for cortical
792 bone. An automatic split at otsu threshold for each bone was collect first, and then mean
793 threshold for a whole cohort was calculated. This average threshold was applied to each
794 bone to normalize bone volume fraction and mineral content.

795

796 **Statistics.** We calculated the minimal animal number required for studies based on the mean
797 and SD values to make sure we had adequate animals per group to address our hypothesis.
798 All the mice were randomly assigned to the indicated groups. Although the investigators
799 responsible for group allocation were not blinded to the allocation scheme, they were blinded
800 to group allocation during data collection, and the investigators responsible for analyses were
801 blinded to the allocation scheme.

802 Significant differences between groups were assessed using a two-sample *t*-test or
803 ANOVA with post-tests as appropriate: one-way ANOVA with Tukey's multiple comparisons
804 test, two-way ANOVA with Sidak's multiple comparisons test and three-way ANOVA analysis

805 as appropriate. All analyses were conducted using the GraphPad Prism version 9. All
806 graphical presentations are mean +/- SD. For statistical comparisons, a *P*-value of < 0.05
807 was considered significant. All experiments were repeated at least twice.

808 **Acknowledgements**

809 This work was supported by grants or fellowships from the NIH to OAM (R01 DK62876; R24
810 DK092759; R01 DK126230; R01 AG069795), SMR (T32 GM835326; F31 DK12272301),
811 DPB (T32 HD007505; T32 GM007863), KS (R01DK115583), KTL (T32 DK071212; F32
812 DK122654), RLS (T32 DK101357; F32 DK123887), KDH (R01AR066028), and CJR
813 (R24DK092759). ZL was supported by a fellowship from the American Diabetes Association
814 (1-18-PDF-087) and EB from the American Heart Association (20-PAF00361). This research
815 was also supported by a Pilot & Feasibility grant and core facilities of the Michigan Integrative
816 Musculoskeletal Health Core Center (P30 AR069620), Michigan Diabetes Research Center
817 (P30 DK020572), Michigan Nutrition and Obesity Center (P30 DK089503), and University of
818 Michigan Comprehensive Cancer Center (P30 CA046592).

819

820 **Author contributions**

821 ZL, KS, KDH, CJR, and OAM conceived the studies and planned the experimental design.
822 ZL, JH, JZ, EB, DPB, HM, KG, KTL, RLS, SMR, and SA performed the experiments. ZL, HY,
823 and OAM analyzed the data. ZL and OAM wrote the manuscript, while all other authors
824 edited and approved the final manuscript.

825

826 **Declaration of Interests**

827 The authors declare no conflicting interests.

828 **References**

- 829 Adamek, G., Felix, R., Guenther, H. L., & Fleisch, H. (1987). Fatty acid oxidation in bone
830 tissue and bone cells in culture. Characterization and hormonal influences. *Biochem*
831 *J*, 248(1), 129-137. doi:10.1042/bj2480129
- 832 Ahmadian, M., Abbott, M. J., Tang, T., Hudak, C. S., Kim, Y., Bruss, M., . . . Sul, H. S. (2011).
833 Desnutrin/ATGL is regulated by AMPK and is required for a brown adipose
834 phenotype. *Cell Metab*, 13(6), 739-748. doi:10.1016/j.cmet.2011.05.002
- 835 Ambrosi, T. H., Scialdone, A., Graja, A., Gohlke, S., Jank, A. M., Bocian, C., . . . Schulz, T. J.
836 (2017). Adipocyte Accumulation in the Bone Marrow during Obesity and Aging
837 Impairs Stem Cell-Based Hematopoietic and Bone Regeneration. *Cell Stem Cell*,
838 20(6), 771-784 e776. doi:10.1016/j.stem.2017.02.009
- 839 Bozec, A., Bakiri, L., Jimenez, M., Rosen, E. D., Catala-Lehnen, P., Schinke, T., . . . Wagner,
840 E. F. (2013). Osteoblast-specific expression of Fra-2/AP-1 controls adiponectin and
841 osteocalcin expression and affects metabolism. *J Cell Sci*, 126(Pt 23), 5432-5440.
842 doi:10.1242/jcs.134510
- 843 Cawthorn, W. P., Scheller, E. L., Learman, B. S., Parlee, S. D., Simon, B. R., Mori, H., . . .
844 MacDougald, O. A. (2014). Bone marrow adipose tissue is an endocrine organ that
845 contributes to increased circulating adiponectin during caloric restriction. *Cell Metab*,
846 20(2), 368-375. doi:10.1016/j.cmet.2014.06.003
- 847 Chen, J., & Long, F. (2013). beta-catenin promotes bone formation and suppresses bone
848 resorption in postnatal growing mice. *J Bone Miner Res*, 28(5), 1160-1169.
849 doi:10.1002/jbmr.1834
- 850 Cook, J. R., & Semple, R. K. (2010). Hypoadiponectinemia--cause or consequence of human
851 "insulin resistance"? *J Clin Endocrinol Metab*, 95(4), 1544-1554. doi:10.1210/jc.2009-
852 2286

- 853 Corsa, C. A. S., Walsh, C. M., Bagchi, D. P., Foss Freitas, M. C., Li, Z., Hardij, J., . . .
854 MacDougald, O. A. (2021). Adipocyte-specific deletion of lamin A/C largely models
855 human familial partial lipodystrophy type 2. *Diabetes*. doi:10.2337/db20-1001
- 856 Devlin, M. J., Cloutier, A. M., Thomas, N. A., Panus, D. A., Lotinun, S., Pinz, I., . . . Boussein,
857 M. L. (2010). Caloric restriction leads to high marrow adiposity and low bone mass in
858 growing mice. *J Bone Miner Res*, 25(9), 2078-2088. doi:10.1002/jbmr.82
- 859 Duchamp de Lageneste, O., Julien, A., Abou-Khalil, R., Frangi, G., Carvalho, C., Cagnard,
860 N., . . . Colnot, C. (2018). Periosteum contains skeletal stem cells with high bone
861 regenerative potential controlled by Periostin. *Nat Commun*, 9(1), 773.
862 doi:10.1038/s41467-018-03124-z
- 863 Eguchi, J., Wang, X., Yu, S., Kershaw, E. E., Chiu, P. C., Dushay, J., . . . Rosen, E. D.
864 (2011). Transcriptional control of adipose lipid handling by IRF4. *Cell Metab*, 13(3),
865 249-259. doi:10.1016/j.cmet.2011.02.005
- 866 Fan, Y., Hanai, J. I., Le, P. T., Bi, R., Maridas, D., DeMambro, V., . . . Lanske, B. (2017).
867 Parathyroid Hormone Directs Bone Marrow Mesenchymal Cell Fate. *Cell Metab*,
868 25(3), 661-672. doi:10.1016/j.cmet.2017.01.001
- 869 Fatayerji, D., & Eastell, R. (1999). Age-related changes in bone turnover in men. *J Bone*
870 *Miner Res*, 14(7), 1203-1210. doi:10.1359/jbmr.1999.14.7.1203
- 871 Fazeli, P. K., Bredella, M. A., Pachon-Pena, G., Zhao, W., Zhang, X., Faje, A. T., . . .
872 Klibanski, A. (2021). The dynamics of human bone marrow adipose tissue in
873 response to feeding and fasting. *JCI Insight*, 6(12). doi:10.1172/jci.insight.138636
- 874 Ferguson, V. L., Ayers, R. A., Bateman, T. A., & Simske, S. J. (2003). Bone development and
875 age-related bone loss in male C57BL/6J mice. *Bone*, 33(3), 387-398.
876 doi:10.1016/s8756-3282(03)00199-6

- 877 Horowitz, M. C., Berry, R., Holtrup, B., Sebo, Z., Nelson, T., Fretz, J. A., . . . Rosen, C. J.
878 (2017). Bone marrow adipocytes. *Adipocyte*, 6(3), 193-204.
879 doi:10.1080/21623945.2017.1367881
- 880 Ito, K., Carracedo, A., Weiss, D., Arai, F., Ala, U., Avigan, D. E., . . . Pandolfi, P. P. (2012). A
881 PML-PPAR-delta pathway for fatty acid oxidation regulates hematopoietic stem cell
882 maintenance. *Nat Med*, 18(9), 1350-1358. doi:10.1038/nm.2882
- 883 Jeon, J. H., Hong, C. W., Kim, E. Y., & Lee, J. M. (2020). Current Understanding on the
884 Metabolism of Neutrophils. *Immune Netw*, 20(6), e46. doi:10.4110/in.2020.20.e46
- 885 Kevorkova, O., Martineau, C., Martin-Falstrault, L., Sanchez-Dardon, J., Brissette, L., &
886 Moreau, R. (2013). Low-bone-mass phenotype of deficient mice for the cluster of
887 differentiation 36 (CD36). *PLoS One*, 8(10), e77701.
888 doi:10.1371/journal.pone.0077701
- 889 Kim, S. P., Li, Z., Zoch, M. L., Frey, J. L., Bowman, C. E., Kushwaha, P., . . . Riddle, R. C.
890 (2017). Fatty acid oxidation by the osteoblast is required for normal bone acquisition
891 in a sex- and diet-dependent manner. *JCI Insight*, 2(16). doi:10.1172/jci.insight.92704
- 892 Kricun, M. E. (1985). Red-yellow marrow conversion: its effect on the location of some
893 solitary bone lesions. *Skeletal Radiol*, 14(1), 10-19. doi:10.1007/BF00361188
- 894 Lee, M. K. S., Al-Sharea, A., Dragoljevic, D., & Murphy, A. J. (2018). Hand of FATE: lipid
895 metabolism in hematopoietic stem cells. *Curr Opin Lipidol*, 29(3), 240-245.
896 doi:10.1097/MOL.0000000000000500
- 897 Lewis, J. W., Edwards, J. R., Naylor, A. J., & McGettrick, H. M. (2021). Adiponectin signalling
898 in bone homeostasis, with age and in disease. *Bone Res*, 9(1), 1.
899 doi:10.1038/s41413-020-00122-0
- 900 Li, N., Zhao, S., Zhang, Z., Zhu, Y., Gliniak, C. M., Vishvanath, L., . . . Scherer, P. E. (2021).
901 Adiponectin preserves metabolic fitness during aging. *Elife*, 10.
902 doi:10.7554/eLife.65108

- 903 Li, Z., Hardij, J., Bagchi, D. P., Scheller, E. L., & MacDougald, O. A. (2018). Development,
904 regulation, metabolism and function of bone marrow adipose tissues. *Bone*, *110*, 134-
905 140. doi:10.1016/j.bone.2018.01.008
- 906 Li, Z., Hardij, J., Evers, S. S., Hutch, C. R., Choi, S. M., Shao, Y., . . . MacDougald, O. A.
907 (2019). G-CSF partially mediates effects of sleeve gastrectomy on the bone marrow
908 niche. *J Clin Invest*, *129*(6), 2404-2416. doi:10.1172/JCI126173
- 909 Li, Z., & MacDougald, O. A. (2021). Preclinical models for investigating how bone marrow
910 adipocytes influence bone and hematopoietic cellularity. *Best Pract Res Clin*
911 *Endocrinol Metab*, 101547. doi:10.1016/j.beem.2021.101547
- 912 Litosch, I., Hudson, T. H., Mills, I., Li, S. Y., & Fain, J. N. (1982). Forskolin as an activator of
913 cyclic AMP accumulation and lipolysis in rat adipocytes. *Mol Pharmacol*, *22*(1), 109-
914 115. Retrieved from <https://www.ncbi.nlm.nih.gov/pubmed/6289066>
- 915 Logan, M., Martin, J. F., Nagy, A., Lobe, C., Olson, E. N., & Tabin, C. J. (2002). Expression
916 of Cre Recombinase in the developing mouse limb bud driven by a Prxl enhancer.
917 *Genesis*, *33*(2), 77-80. doi:10.1002/gene.10092
- 918 Maridas, D. E., Rendina-Ruedy, E., Helderman, R. C., DeMambro, V. E., Brooks, D., Guntur,
919 A. R., . . . Rosen, C. J. (2019). Progenitor recruitment and adipogenic lipolysis
920 contribute to the anabolic actions of parathyroid hormone on the skeleton. *FASEB J*,
921 *33*(2), 2885-2898. doi:10.1096/fj.201800948RR
- 922 McIlroy, G. D., Suchacki, K., Roelofs, A. J., Yang, W., Fu, Y., Bai, B., . . . Rochford, J. J.
923 (2018). Adipose specific disruption of seipin causes early-onset generalised
924 lipodystrophy and altered fuel utilisation without severe metabolic disease. *Mol Metab*,
925 *10*, 55-65. doi:10.1016/j.molmet.2018.01.019
- 926 Merceron, C., Mangiavini, L., Robling, A., Wilson, T. L., Giaccia, A. J., Shapiro, I. M., . . .
927 Risbud, M. V. (2014). Loss of HIF-1alpha in the notochord results in cell death and

- 928 complete disappearance of the nucleus pulposus. *PLoS One*, 9(10), e110768.
929 doi:10.1371/journal.pone.0110768
- 930 Mizoguchi, T., Pinho, S., Ahmed, J., Kunisaki, Y., Hanoun, M., Mendelson, A., . . . Frenette,
931 P. S. (2014). Osterix marks distinct waves of primitive and definitive stromal
932 progenitors during bone marrow development. *Dev Cell*, 29(3), 340-349.
933 doi:10.1016/j.devcel.2014.03.013
- 934 Mori, H., Dugan, C. E., Nishii, A., Benchamana, A., Li, Z., Cadenhead, T. S. t., . . .
935 MacDougald, O. A. (2021). The molecular and metabolic program by which white
936 adipocytes adapt to cool physiologic temperatures. *PLoS Biol*, 19(5), e3000988.
937 doi:10.1371/journal.pbio.3000988
- 938 Morse, A., McDonald, M. M., Kelly, N. H., Melville, K. M., Schindeler, A., Kramer, I., . . . Little,
939 D. G. (2014). Mechanical load increases in bone formation via a sclerostin-
940 independent pathway. *J Bone Miner Res*, 29(11), 2456-2467. doi:10.1002/jbmr.2278
- 941 Mottillo, E. P., Bloch, A. E., Leff, T., & Granneman, J. G. (2012). Lipolytic products activate
942 peroxisome proliferator-activated receptor (PPAR) alpha and delta in brown
943 adipocytes to match fatty acid oxidation with supply. *J Biol Chem*, 287(30), 25038-
944 25048. doi:10.1074/jbc.M112.374041
- 945 Mukohira, H., Hara, T., Abe, S., Tani-Ichi, S., Sehara-Fujisawa, A., Nagasawa, T., . . . Ikuta,
946 K. (2019). Mesenchymal stromal cells in bone marrow express adiponectin and are
947 efficiently targeted by an adiponectin promoter-driven Cre transgene. *Int Immunol*,
948 31(11), 729-742. doi:10.1093/intimm/dxz042
- 949 Muzumdar, M. D., Tasic, B., Miyamichi, K., Li, L., & Luo, L. (2007). A global double-
950 fluorescent Cre reporter mouse. *Genesis*, 45(9), 593-605. doi:10.1002/dvg.20335
- 951 Naot, D., Watson, M., Callon, K. E., Tuari, D., Musson, D. S., Choi, A. J., . . . Cornish, J.
952 (2016). Reduced Bone Density and Cortical Bone Indices in Female Adiponectin-
953 Knockout Mice. *Endocrinology*, 157(9), 3550-3561. doi:10.1210/en.2016-1059

- 954 Naveiras, O., Nardi, V., Wenzel, P. L., Hauschka, P. V., Fahey, F., & Daley, G. Q. (2009).
955 Bone-marrow adipocytes as negative regulators of the haematopoietic
956 microenvironment. *Nature*, *460*(7252), 259-263. doi:10.1038/nature08099
- 957 Polineni, S., Resulaj, M., Faje, A. T., Meenaghan, E., Bredella, M. A., Bouxsein, M., . . .
958 Fazeli, P. K. (2020). Red and White Blood Cell Counts Are Associated With Bone
959 Marrow Adipose Tissue, Bone Mineral Density, and Bone Microarchitecture in
960 Premenopausal Women. *J Bone Miner Res*, *35*(6), 1031-1039. doi:10.1002/jbmr.3986
- 961 Ran, F. A., Hsu, P. D., Wright, J., Agarwala, V., Scott, D. A., & Zhang, F. (2013). Genome
962 engineering using the CRISPR-Cas9 system. *Nat Protoc*, *8*(11), 2281-2308.
963 doi:10.1038/nprot.2013.143
- 964 Raymond, C. S., & Soriano, P. (2007). High-efficiency FLP and PhiC31 site-specific
965 recombination in mammalian cells. *PLoS One*, *2*(1), e162.
966 doi:10.1371/journal.pone.0000162
- 967 Riddle, R. C., & Clemens, T. L. (2017). Bone Cell Bioenergetics and Skeletal Energy
968 Homeostasis. *Physiol Rev*, *97*(2), 667-698. doi:10.1152/physrev.00022.2016
- 969 Robles, H., Park, S., Joens, M. S., Fitzpatrick, J. A. J., Craft, C. S., & Scheller, E. L. (2019).
970 Characterization of the bone marrow adipocyte niche with three-dimensional electron
971 microscopy. *Bone*, *118*, 89-98. doi:10.1016/j.bone.2018.01.020
- 972 Rolfe, D. F., & Brown, G. C. (1997). Cellular energy utilization and molecular origin of
973 standard metabolic rate in mammals. *Physiol Rev*, *77*(3), 731-758.
974 doi:10.1152/physrev.1997.77.3.731
- 975 Roy, I. M., Biswas, A., Verfaillie, C., & Khurana, S. (2018). Energy Producing Metabolic
976 Pathways in Functional Regulation of the Hematopoietic Stem Cells. *IUBMB Life*,
977 *70*(7), 612-624. doi:10.1002/iub.1870
- 978 Scheller, E. L., Doucette, C. R., Learman, B. S., Cawthorn, W. P., Khandaker, S., Schell,
979 B., . . . MacDougald, O. A. (2015). Region-specific variation in the properties of

- 980 skeletal adipocytes reveals regulated and constitutive marrow adipose tissues. *Nat*
981 *Commun*, 6, 7808. doi:10.1038/ncomms8808
- 982 Scheller, E. L., Khandaker, S., Learman, B. S., Cawthorn, W. P., Anderson, L. M., Pham, H.
983 A., . . . MacDougald, O. A. (2019). Bone marrow adipocytes resist lipolysis and
984 remodeling in response to beta-adrenergic stimulation. *Bone*, 118, 32-41.
985 doi:10.1016/j.bone.2018.01.016
- 986 Schoiswohl, G., Stefanovic-Racic, M., Menke, M. N., Wills, R. C., Surlow, B. A., Basantani,
987 M. K., . . . Kershaw, E. E. (2015). Impact of Reduced ATGL-Mediated Adipocyte
988 Lipolysis on Obesity-Associated Insulin Resistance and Inflammation in Male Mice.
989 *Endocrinology*, 156(10), 3610-3624. doi:10.1210/en.2015-1322
- 990 Shen, W., Chen, J., Punyanitya, M., Shapses, S., Heshka, S., & Heymsfield, S. B. (2007).
991 MRI-measured bone marrow adipose tissue is inversely related to DXA-measured
992 bone mineral in Caucasian women. *Osteoporos Int*, 18(5), 641-647.
993 doi:10.1007/s00198-006-0285-9
- 994 Valet, C., Batut, A., Vauclard, A., Dortignac, A., Bellio, M., Payrastre, B., . . . Severin, S.
995 (2020). Adipocyte Fatty Acid Transfer Supports Megakaryocyte Maturation. *Cell Rep*,
996 32(1), 107875. doi:10.1016/j.celrep.2020.107875
- 997 Vogler, J. B., 3rd, & Murphy, W. A. (1988). Bone marrow imaging. *Radiology*, 168(3), 679-
998 693. doi:10.1148/radiology.168.3.3043546
- 999 Wang, F., Mullican, S. E., DiSpirito, J. R., Peed, L. C., & Lazar, M. A. (2013). Lipoatrophy and
1000 severe metabolic disturbance in mice with fat-specific deletion of PPARgamma. *Proc*
1001 *Natl Acad Sci U S A*, 110(46), 18656-18661. doi:10.1073/pnas.1314863110
- 1002 Yang, J., Park, O. J., Kim, J., Han, S., Yang, Y., Yun, C. H., & Han, S. H. (2019). Adiponectin
1003 Deficiency Triggers Bone Loss by Up-Regulation of Osteoclastogenesis and Down-
1004 Regulation of Osteoblastogenesis. *Front Endocrinol (Lausanne)*, 10, 815.
1005 doi:10.3389/fendo.2019.00815

- 1006 Zhou, B. O., Yu, H., Yue, R., Zhao, Z., Rios, J. J., Naveiras, O., & Morrison, S. J. (2017).
1007 Bone marrow adipocytes promote the regeneration of stem cells and haematopoiesis
1008 by secreting SCF. *Nat Cell Biol*, 19(8), 891-903. doi:10.1038/ncb3570
- 1009 Zou, W., Rohatgi, N., Brestoff, J. R., Li, Y., Barve, R. A., Tycksen, E., . . . Teitelbaum, S. L.
1010 (2020). Ablation of Fat Cells in Adult Mice Induces Massive Bone Gain. *Cell Metab*,
1011 32(5), 801-813 e806. doi:10.1016/j.cmet.2020.09.011
- 1012 Zou, W., Rohatgi, N., Brestoff, J. R., Zhang, Y., Scheller, E. L., Craft, C. S., . . . Teitelbaum,
1013 S. L. (2019). Congenital lipodystrophy induces severe osteosclerosis. *PLoS Genet*,
1014 15(6), e1008244. doi:10.1371/journal.pgen.1008244

1015

1016 **Figures and figure supplement list:**

1017 Figure 1 is associated with 2 supplements:

1018 Figure 1 - figure supplement 1

1019 Figure 1 - figure supplement 2

1020 Figure 3 is associated with 4 supplements:

1021 Figure 3 - figure supplement 1

1022 Figure 3 - figure supplement 2

1023 Figure 3 - figure supplement 3

1024 Figure 3 - figure supplement 4

1025 Figure 4 is associated with 1 supplement:

1026 Figure 4 - figure supplement 1

1027 Figure 5 is associated with 2 supplements:

1028 Figure 5 - figure supplement 1

1029 Figure 5 - figure supplement 2

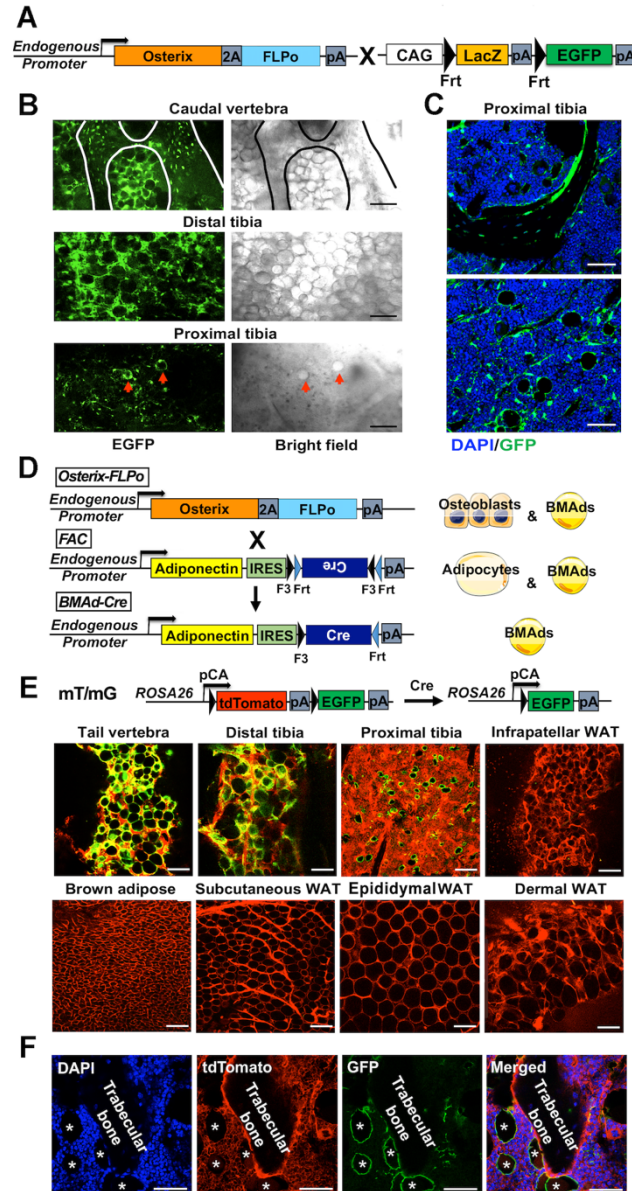


Figure 1. Generation of a BMAd-specific Cre mouse model (BMAd-Cre).

A. Efficacy of *Osterix-FLPo* evaluated by crossing with FLP-dependent EGFP reporter to yield *Osterix-EGFP*.

B. *Osterix-EGFP* male mice at 16 weeks were sacrificed. Fresh tissue confocal microscopy was performed on bisected caudal vertebrae, distal tibia and proximal tibia. Red arrows indicate singly dispersed BMAds. Scale bar; 100 μ m.

C. Frozen-sections of proximal tibiae slides from *Osterix-EGFP* were stained with Anti-GFP (green) and DAPI (blue). Scale bar; 50 μ m.

D. Schematic of how *Osterix-FLPo* recombines FLPo-activated *Adipoq-Cre* (FAC) in BMAd-Cre mice to restrict expression of Cre to BMAds.

E. BMAd-Cre mice were bred with mT/mG reporter mice and resulting BMAd-mT/mG mice were sacrificed at 16 weeks of age and cellular fluorescence evaluated by fresh tissue confocal microscopy. Scale bar; 100 μ m.

F. Proximal tibia sections from BMAd-mT/mG mice were stained with antibodies to tdTomato, (red) and EGFP (green), and nuclei were counterstained with DAPI (blue). * indicates BMAds. Scale bar; 50 μ m.

Figure 1 is associated with 2 supplements: Figure 1 - figure supplement 1; Figure 1 - figure supplement 2.

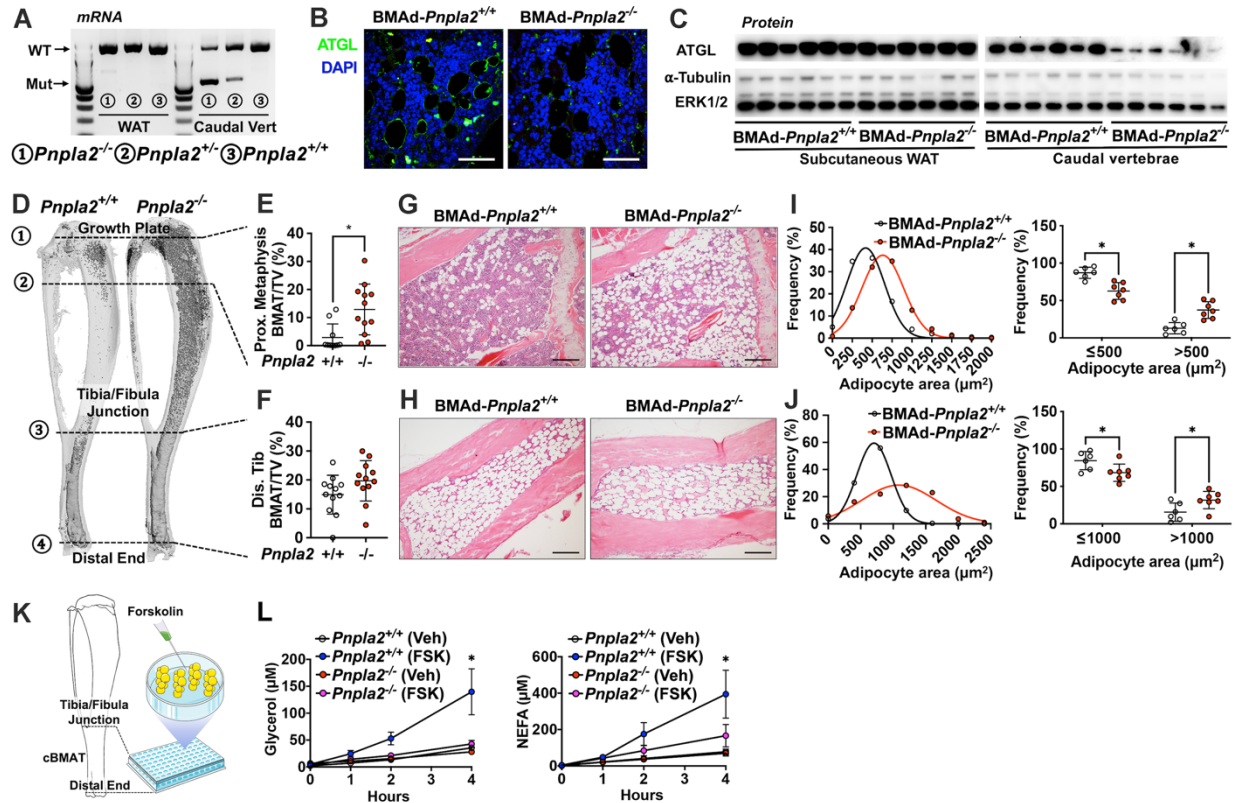


Figure 2. Ablation of adipose triglyceride lipase (ATGL; gene name *Pnpla2*) increases size and number of BMAd.

A-J. Male mice of the indicated genotypes at 24 weeks of age were euthanized for investigation of white adipose tissue (WAT) and bone.

A. RNA was extracted from WAT and caudal vertebrae and converted to cDNA. PCR products for wildtype (WT; 1257bp) *Pnpla2* and exon 2-7 knockout (Mut; 553 bp) bands were visualized.

B. Decalcified proximal tibiae were sectioned and used for immunofluorescent staining for ATGL (green) expression. Slides were counterstained with DAPI (blue) for nuclei. Scale bar; 50 μm.

C. Immunoblot analyses of ATGL, α-tubulin, and ERK1/2 in lysates from subcutaneous WAT and caudal vertebral.

D-F. Decalcified tibiae were stained with osmium tetroxide and visualized by μCT (D). BMAT of proximal (E) and distal (F) tibia was quantified. Data are expressed as mean ± SD. * indicates $P < 0.05$ with a two-sample *t*-test.

G-H. Decalcified tibiae were paraffin-sectioned and stained with Hematoxylin & Eosin. Representative pictures were taken from proximal (G) and distal (H) tibia. Scale bar; 200 μm.

I-J. BMAd sizes from proximal (I) and distal (J) tibiae were quantified with MetaMorph software. Data are expressed as mean ± SD. * indicates $P < 0.05$ with two-way ANOVA with Sidak's multiple comparisons test.

K-L. Distal tibial BMAT was flushed from female BMAd-*Pnpla2*^{-/-} and their wildtype littermates at 24 weeks of age. For each n, distal tibial explants from 2 mice were combined per well and cultured in 2% BSA-HBSS solution (K). Subgroups from each genotype were treated with forskolin (FSK, 5 μM) or vehicle (Veh, DMSO). Released glycerol and non-esterified fatty acid (NEFA) in culture media at indicated time points were measured by colorimetric assay (n = 3-4 per treatment) (L). * indicates *Pnpla2*^{+/+} (FSK) different from *Pnpla2*^{+/+} (Veh) and from *Pnpla2*^{-/-} (FSK) with $P < 0.05$ with two-way ANOVA with Sidak's multiple comparisons test.

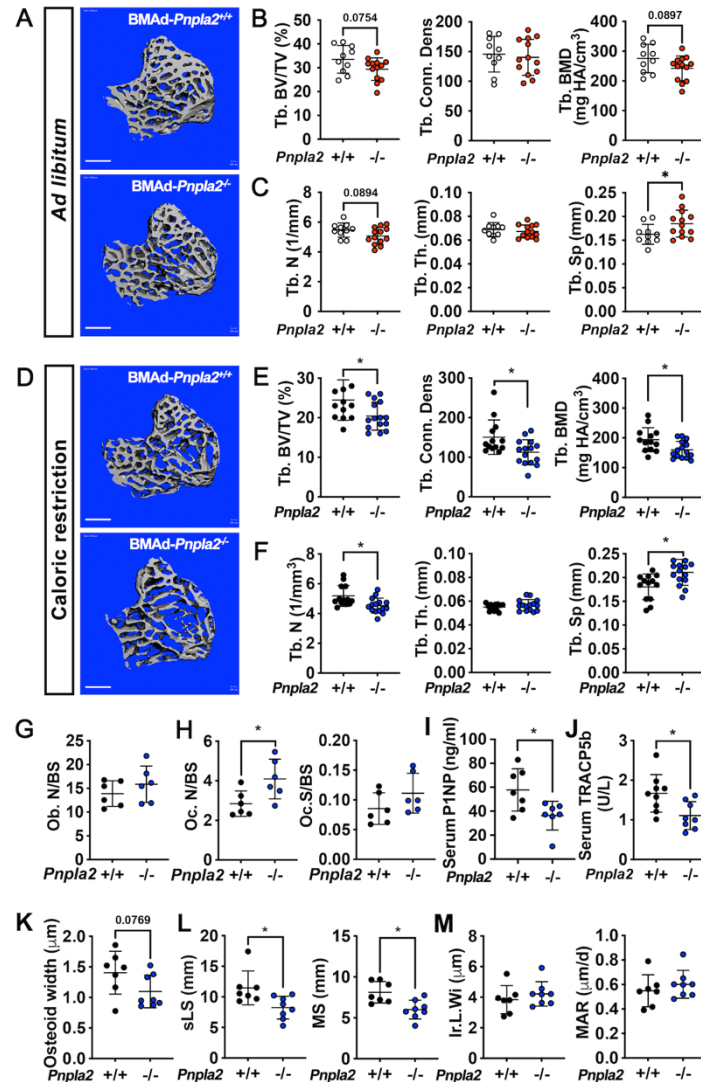


Figure 3. BAd lipolysis is required to maintain bone homeostasis in male mice under CR conditions, but not when mice are fed *ad libitum*.

A-C. Male BMAc-*Pnpla2*^{-/-} and their BMAc-*Pnpla2*^{+/+} littermates with *ad libitum* feeding were euthanized at 24 weeks of age. Tibiae from *ad libitum* mice were analyzed by μ CT for indicated trabecular bone variables. Scale bars indicate 500 μ m.

D-M. Male mice at 18 weeks of age underwent 30% CR for 6 weeks. Two independent age- and sex-matched cohorts were plotted together for μ CT parameters (D-F), one of those two cohorts was used for ELISA, and static or dynamic histomorphometry (G-M).

D-F. Tibiae from CR mice were analyzed by μ CT for indicated trabecular bone variables. Scale bar; 500 μ m.

G-H. Static histomorphometry analyses were performed to calculate osteoblast number (Ob. N), osteoclast number (Oc. N) and osteoclast surface (Oc. S) per bone surface (BS).

I-J. Concentrations of circulating P1NP and TRACP5b in CR mice.

K. Osteoid quantification was performed on undecalcified plastic sections with Goldner's Trichrome staining.

L-M. Dynamic histomorphometry was performed on calcein-labelled trabecular bone from proximal tibia. sLS: single-labelled surface; MS: mineralized surface; Ir.L.Wi: inter-label width; MAR: mineral apposition rate. Data are expressed as mean \pm SD. * indicates $P < 0.05$ with a two-sample t -test.

Figure 3 is associated with 4 supplements: Figure 3 - figure supplement 1; Figure 3 - figure supplement 2; Figure 3 - figure supplement 3; Figure 3 - figure supplement 4.

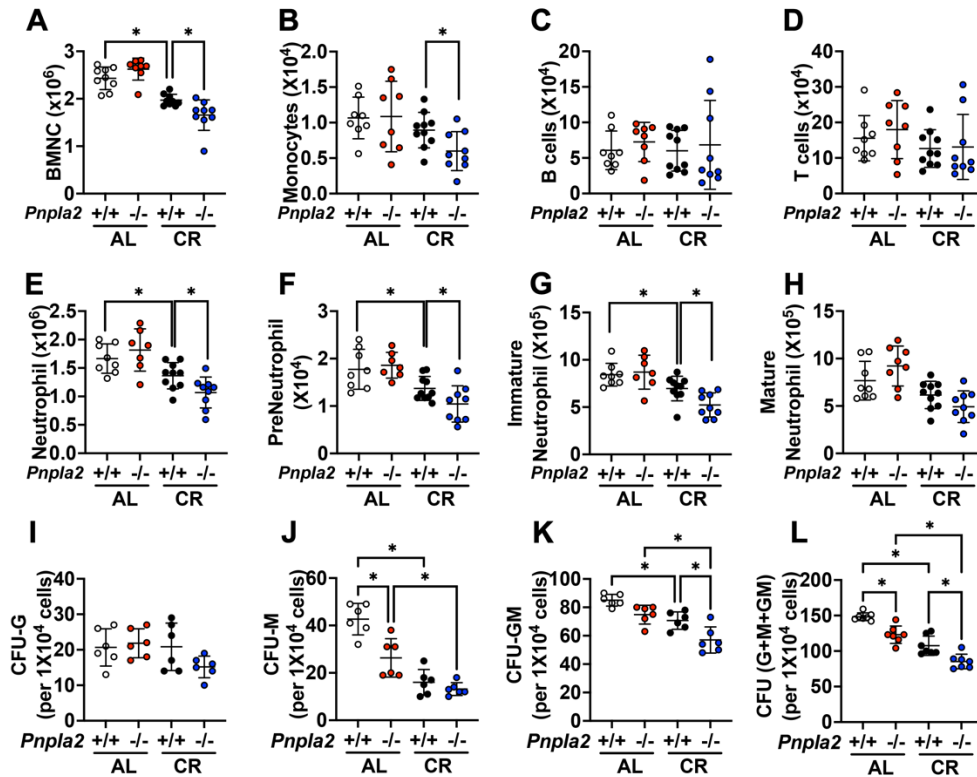


Figure 4. BMAde-*Pnpla2* deficiency impairs myelopoiesis.

A-H. BMAde-*Pnpla2*^{-/-} mice and littermate controls (*Pnpla2*^{+/+}) were caloric restricted (CR) for 20 weeks or remained on an *ad libitum* (AL) diet, and then received whole-body irradiation (6 Gy). Mice were euthanized 9 days post-irradiation. Femurs were collected for flow cytometry to measure the regeneration of hematopoietic cells. Bone marrow mononuclear cells (BMNCs), monocytes, B and T lymphocytes and neutrophils were quantified.

I-L. CFU assays. Femora and tibial bone marrow cells were isolated from BMAde-*Pnpla2*^{-/-} mice and littermate controls (*Pnpla2*^{+/+}), which had been fed *ad libitum* (AL) or a caloric restricted (CR) diet for 20 weeks. After counting, 1x10⁴ cells were plated for CFU assays. Colonies were counted by an independent expert in a blinded manner 7 days after plating.

Data are expressed as mean ± SD. * indicates $P < 0.05$ with one-way ANOVA with Tukey's multiple comparisons test.

Figure 4 is associated with 1 supplement: Figure 4 - figure supplement 1.

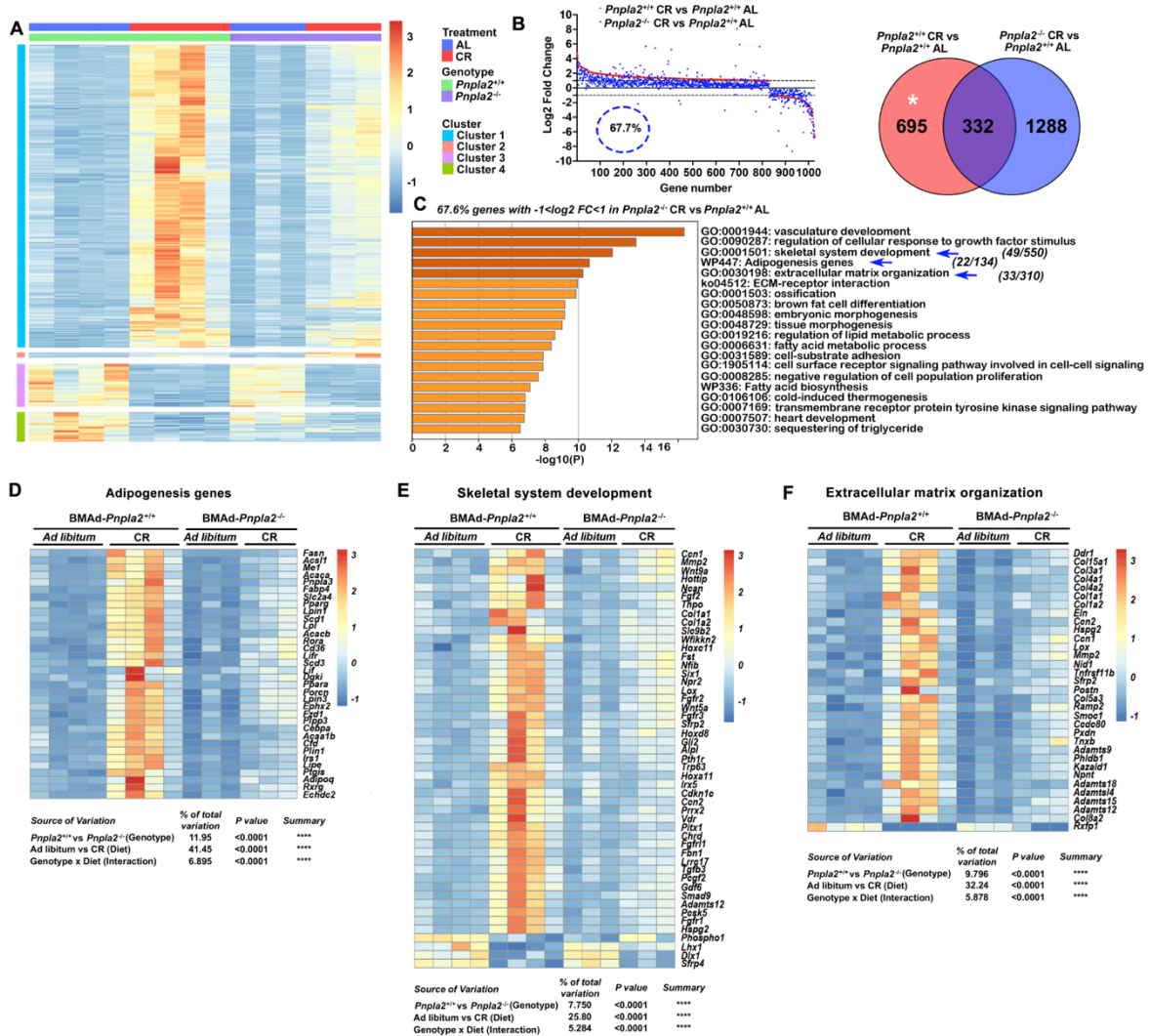


Figure 5. BMAd-*Pnpla2* deficiency causes extensive alterations to the bone marrow transcriptome only when coupled with CR.

Male control and BMAd-*Pnpla2*^{-/-} mice at 24 weeks of age were either fed AL or underwent 30% CR for 6 weeks. Distal tibial cBMAT was flushed and cBMAT from two mice was pooled as one sample for RNAseq analyses (n of 3 or 4 per treatment).

A. Differential genes with our criteria ($P_{adj} < 0.05$ and $|\text{Log}_2 \text{fold change}| > 1$) between BMAd-*Pnpla2*^{+/+} CR and BMAd-*Pnpla2*^{+/+} ad libitum (AL) were grouped into 4 clusters.

B. Genes different between BMAd-*Pnpla2*^{+/+} CR and BMAd-*Pnpla2*^{+/+} AL were ordered from maximum to minimum \log_2 fold change (red dots), and compared to corresponding data from BMAd-*Pnpla2*^{-/-} CR versus BMAd-*Pnpla2*^{-/-} AL (blue dots). Venn diagram shows the differential genes between BMAd-*Pnpla2*^{+/+} CR versus BMAd-*Pnpla2*^{+/+} AL BMAT; and BMAd-*Pnpla2*^{-/-} CR versus BMAd-*Pnpla2*^{+/+} AL BMAT.

C. Pathway analyses of genes significantly changed by CR in BMAd-*Pnpla2*^{+/+} mice, but not in CR mice lacking *Pnpla2* (indicated by * area in panel B). Pathways further analyzed by heatmap indicated with blue arrows.

D-F. Expression Z-scores of genes related to adipogenesis (D), skeletal system development (E) and extracellular matrix organization (F) were shown as heatmap. Effects of genotype and diet, and their interactions were analyzed by three-way ANOVA.

Figure 5 is associated with 2 supplements: Figure 5 - figure supplement 1; Figure 5 - figure supplement 2.

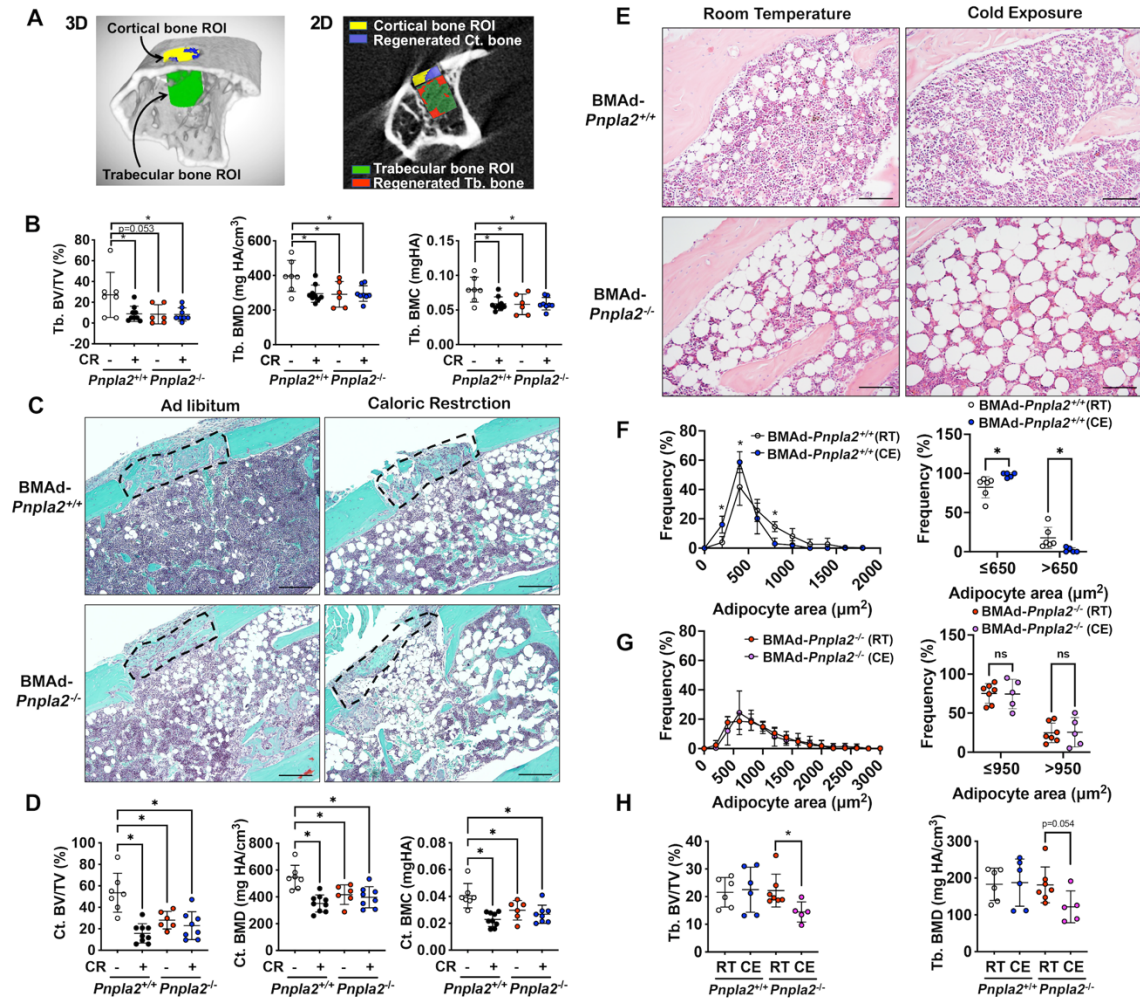


Figure 6. Energy from BMAd is required for trabecular bone regeneration and protects against bone loss caused by chronic cold exposure.

A-D. BMAd-*Pnpla2*^{+/+} and BMAd-*Pnpla2*^{-/-} male mice at 24 weeks of age fed with chow diet (-) or underwent 30% CR for 6 weeks (+). A 0.7 mm proximal tibial defect was created 1 to 2 mm distal to the growth plate. Tibiae were collected 9 days after surgery. MicroCT was performed to analyze trabecular and cortical bone regeneration.

A. Representative analyzing images of bone defect. Example of μ CT showing trabecular bone region of interest (ROI; green) and newly generated trabecular bone (red); cortical bone ROI (yellow) and newly formed cortical bone (purple).

B. Quantification of regenerated trabecular bone volume fraction (BV/TV), mineral density (BMD) and mineral content (BMC). Data are expressed as mean \pm SD. * indicates $P < 0.05$ with one-way ANOVA with Tukey's multiple comparisons test.

C. Safranin O/ Fast Green (SO/FG) staining of new cortical bone formation in defect sites. Scale bar; 200 μ m.

D. Quantification of regenerated cortical bone volume fraction (BV/TV), mineral density (BMD) and mineral content (BMC). Data are expressed as mean \pm SD. * indicates $P < 0.05$ with one-way ANOVA with Tukey's multiple comparisons test.

E-I. Female BMAd-*Pnpla2*^{+/+} and BMAd-*Pnpla2*^{-/-} mice at 20 weeks of age were singly housed at 5°C for 3 weeks without enrichments. Tibiae were collected for sectioning and μ CT analyses.

E. Proximal tibiae were decalcified and paraffin-sectioned for H&E staining. Representative images for proximal tibia are shown. Scale bar, 100 μ m.

F-G. Quantification of BMAds from H&E-stained slides using MetaMorph software. Comparison of BMAd size at room temperature (RT) versus cold exposure (CE) in mice of indicated genotypes. Data are expressed as mean \pm SD. * indicates $P < 0.05$ with two-way ANOVA with Sidak's multiple comparisons test.

H. Trabecular bone volume fraction (BV/TV) and mineral density (BMD) were quantified by μ CT. Data are expressed as mean \pm SD. * indicates $P < 0.05$ with one-way ANOVA with Tukey's multiple comparisons test.

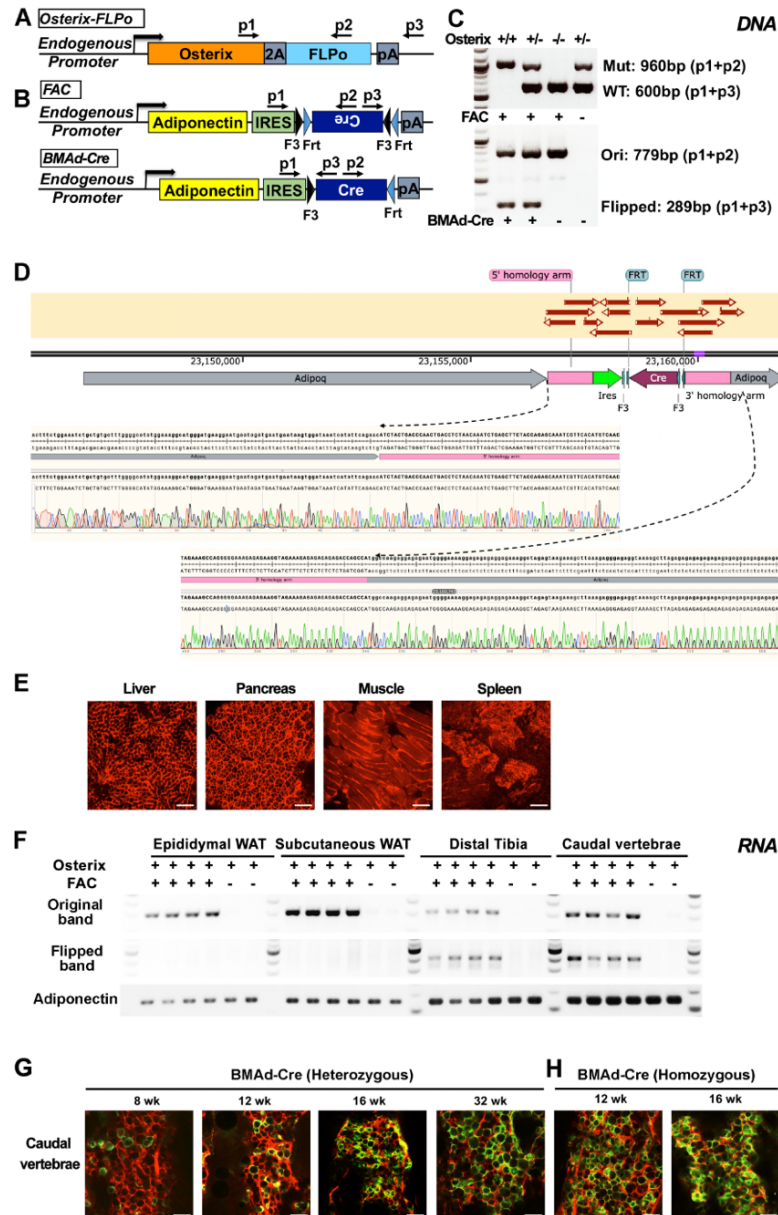


Figure 1 - figure supplement 1. Genotyping strategy and validation of BMAAd-Cre.

A-C. Schematic of genotyping primer designing for *Osterix-FLPo* (A) and FLPo activated *Adipoq-Cre* (FAC; B), and representative genotyping results (C). Mut= Mutation; WT=wildtype; Ori=original band without conversion of reversed Cre cassette; Flipped=FLPo activated Cre (BMAAd-Cre).

D. Representative image of genomic PCR sequencing aligned with the endogenous allele.

E. BMAAd-Cre mice were bred with mT/mG reporter mice and the resulting BMAAd-mT/mG mice were sacrificed at 16 weeks of age. Cellular fluorescence was evaluated by fresh tissue confocal microscopy. Scale bar; 100 μ m.

F. The flipped recombination band is found in mRNA of bone, but not WAT depots. Mice expressing *Osterix-FLPo* with or without FAC were sacrificed and mRNA was isolated. cDNAs from distal tibia, caudal vertebrae, epididymal and subcutaneous WATs were used for PCR and agarose gel electrophoresis.

G, H. Efficiency of BMAAd-Cre recombinase is age- and allele-dependent. Fresh caudal vertebrae collected from BMAAd-mT/mG mice at indicated ages were bisected and used for confocal imaging. Scale bar; 100 μ m.

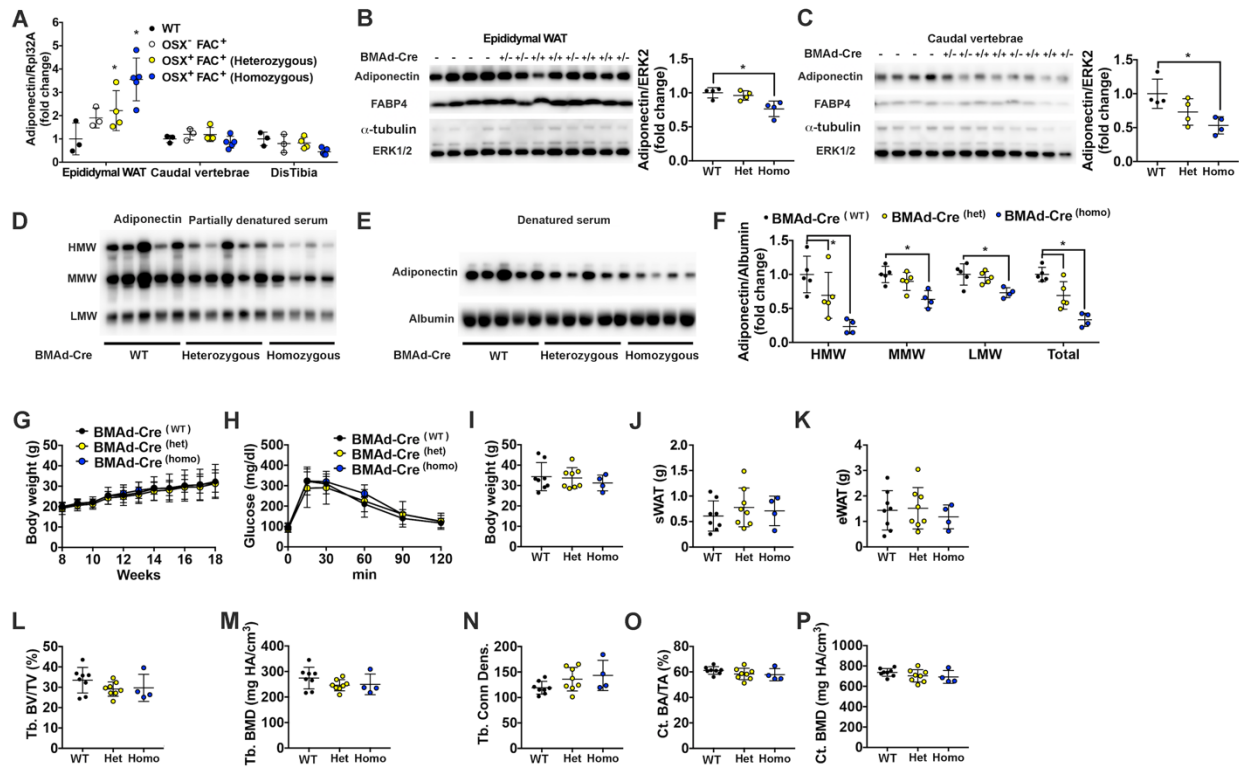


Figure 1 - figure supplement 2. Insertion of IRES-Cre cassette in the 3'UTR of endogenous *Adipoq* decreases expression of adiponectin but does not cause a metabolic or bone phenotype.

A-F. Endogenous adiponectin expression is decreased by IRES-Cre insertion. Mice expressing *Osterix-FLPo* with or without FAC were sacrificed. Epididymal WAT (eWAT), caudal vertebrae, distal tibiae and serum were collected.

A. mRNA expression of adiponectin in eWAT, caudal vertebrae and distal tibiae from BMAd-Cre (OSX⁺FAC⁺) WT, Heterozygous, and Homozygous mice.

B-C. Lysates from eWAT (B) and caudal vertebrae (C) were used for immunoblot analyses of adiponectin and FABP4, with α -tubulin and ERK1/2 as loading controls. Quantification was performed using Image J.

D-F. Non-denatured (D) and denatured (E) serum from BMAd-Cre WT, heterozygous, or homozygous mice was used for immunoblot analyses of adiponectin, with albumin as a reference protein. High, medium and low molecular weight forms of adiponectin were quantified by Image J.

G-P. Hypoadiponectinemia does not cause detectable phenotypes. Male BMAd-Cre WT, heterozygote, or homozygote mice were sacrificed at 18 weeks of age. Soft tissues and bones were collected.

G-K. Body weight, glucose tolerance, and WAT depot weights are not changed in BMAd-Cre mice.

L-P. Trabecular and cortical bone parameters were determined by μ CT.

Data are expressed as mean \pm SD. * indicates $P < 0.05$ with one-way ANOVA with Tukey's multiple comparisons test.

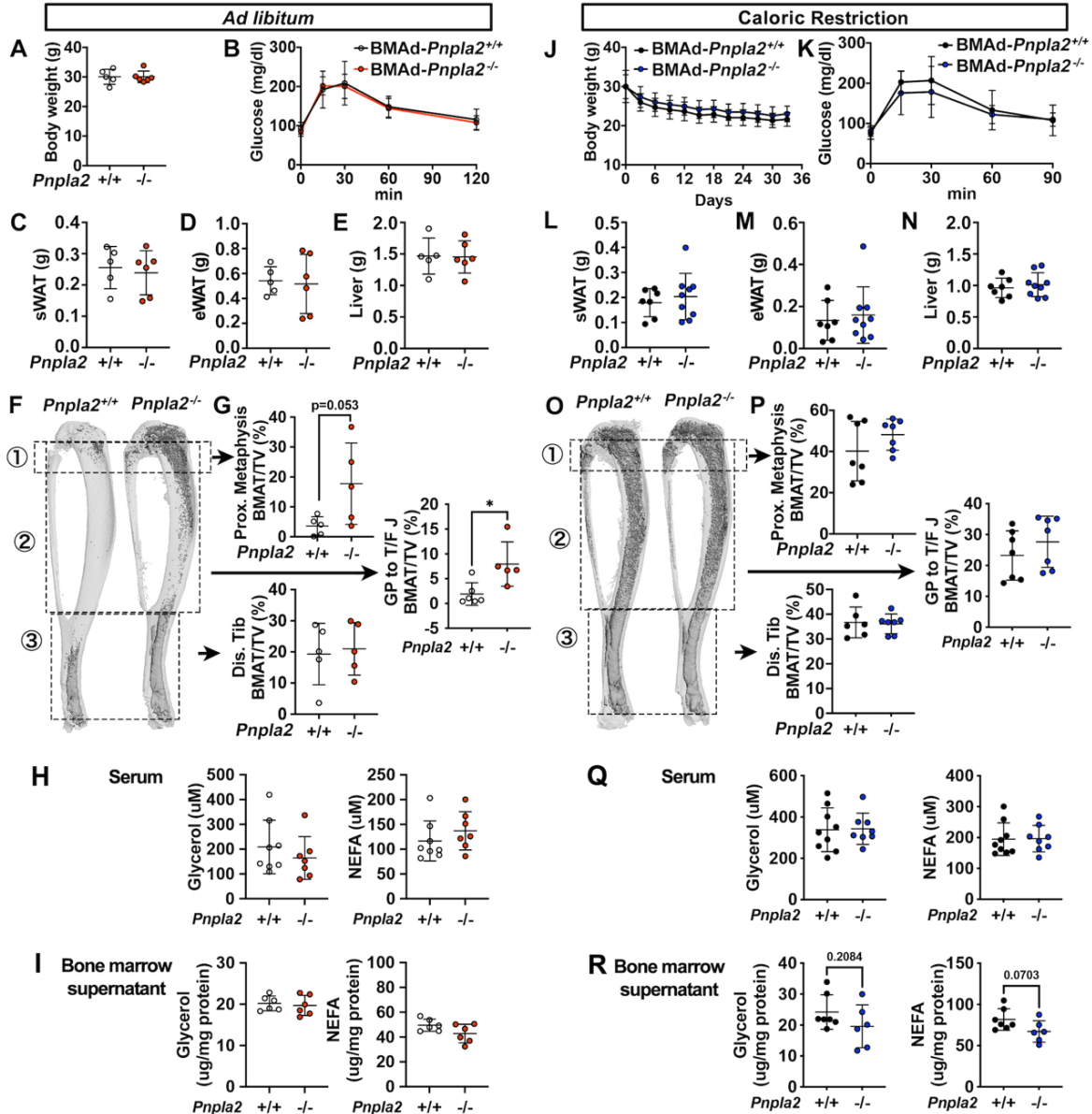


Figure 3 - figure supplement 1. Blocking BMAd-lipolysis does not influence global metabolism when mice are fed *ad libitum* or calorically restricted.

A-I. BMAd-*Pnpla2*^{-/-} male mice and littermate controls (*Pnpla2*^{+/+}) were fed *ad libitum* until 24 weeks of age. Body weight (A), glucose tolerance test (B), and weights of subcutaneous WAT (sWAT), epididymal WAT (eWAT) and liver (C-E) were recorded. Decalcified tibiae were used for osmium tetroxide-staining and quantified by μ CT analyses to measure the BMAT volume at proximal and distal ends, as indicated by boxed regions (F-G). Concentrations of glycerol and NEFA in serum (H) and bone marrow supernatant (I) were measured with colorimetric assay kits. Glycerol and NEFA contents in bone marrow supernatant were normalized to protein concentrations.

J-R. BMAd-*Pnpla2*^{-/-} male mice and littermate controls (*Pnpla2*^{+/+}) at 18 weeks of age and underwent a 30% CR for 6 weeks. Body weight changes (J) and glucose tolerance (K) were recorded. sWAT (L), eWAT (M), and liver (N) weights were measured during dissection. BMAT volume at proximal and distal tibia were quantified in osmium tetroxide-stained bones following μ CT scanning (O-P). Concentrations of glycerol and NEFA in serum (Q) and bone marrow supernatant (R) were measured using colorimetric assays. Glycerol and NEFA contents in bone marrow supernatant were normalized to protein concentrations.

Data are expressed as mean \pm SD. * indicates $P < 0.05$ with a two-sample *t*-test.

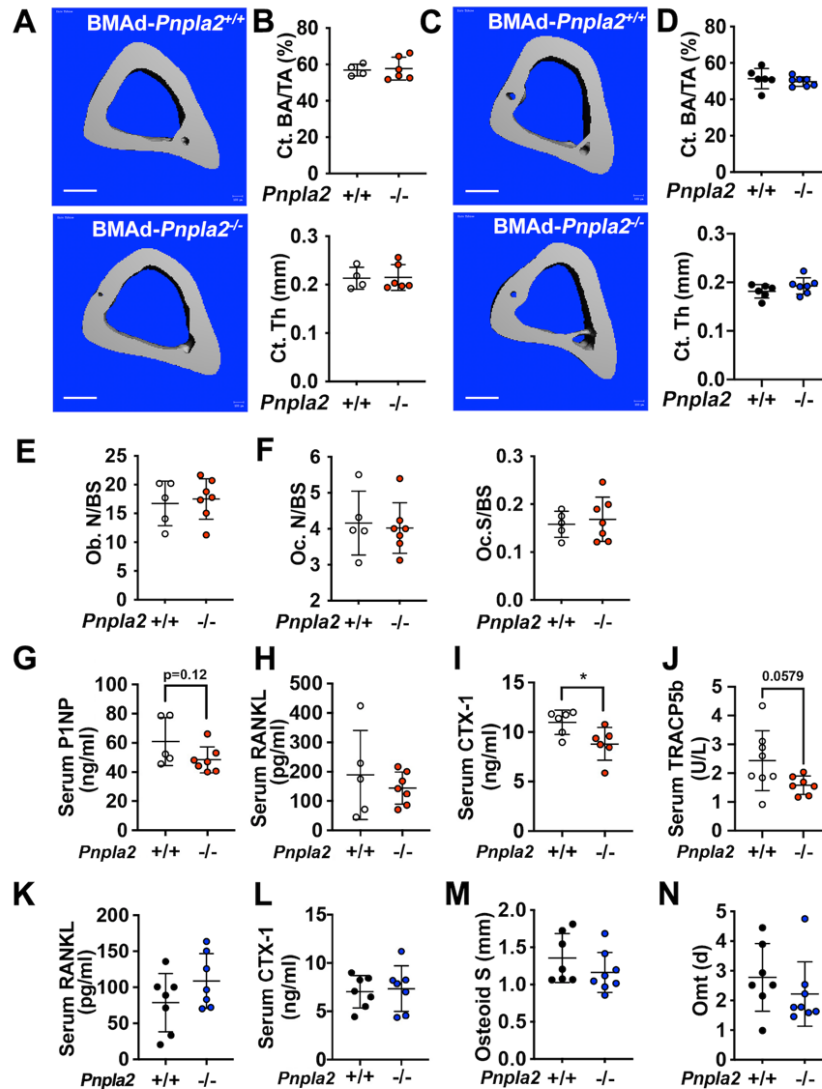


Figure 3 - figure supplement 2. Cortical bone variables in BMAAd-*Pnpla2*^{-/-} mice and other possible mechanisms for bone loss in BMAAd-*Pnpla2*^{-/-} CR mice.

A-D. Mouse tibiae from 24 weeks old *ad libitum* (A-B) or CR (C-D) mice were collected. Cortical bone area (CT. BA/TA) and thickness (Ct. Th) were measured by μ CT. Scale bar; 500 μ m.

E-J. BMAAd-*Pnpla2*^{-/-} male mice and littermate controls (*Pnpla2*^{+/+}) were fed *ad libitum* until 24 weeks of age. E-F. Proximal tibial static histomorphometry was performed to calculate osteoblast number (Ob. N), osteoclast number (Oc. N) and osteoclast surface (Oc. S) per bone surface (BS). G-J. Circulating P1NP, RANKL, CTX-1 and TRACP5b were measured with commercially available ELISA kits.

K-N. BMAAd-*Pnpla2*^{-/-} male mice and littermate controls (*Pnpla2*^{+/+}) at 18 weeks of age underwent a 30% CR for 6 weeks. K-L. Circulating RANKL and CTX-1 were measured with commercially available ELISA kits. M-N. Histomorphometry analysis for osteoid surface and osteoid maturation time (Omt).

Data are expressed as mean \pm SD. * indicates $P < 0.05$ with a two-sample *t*-test.

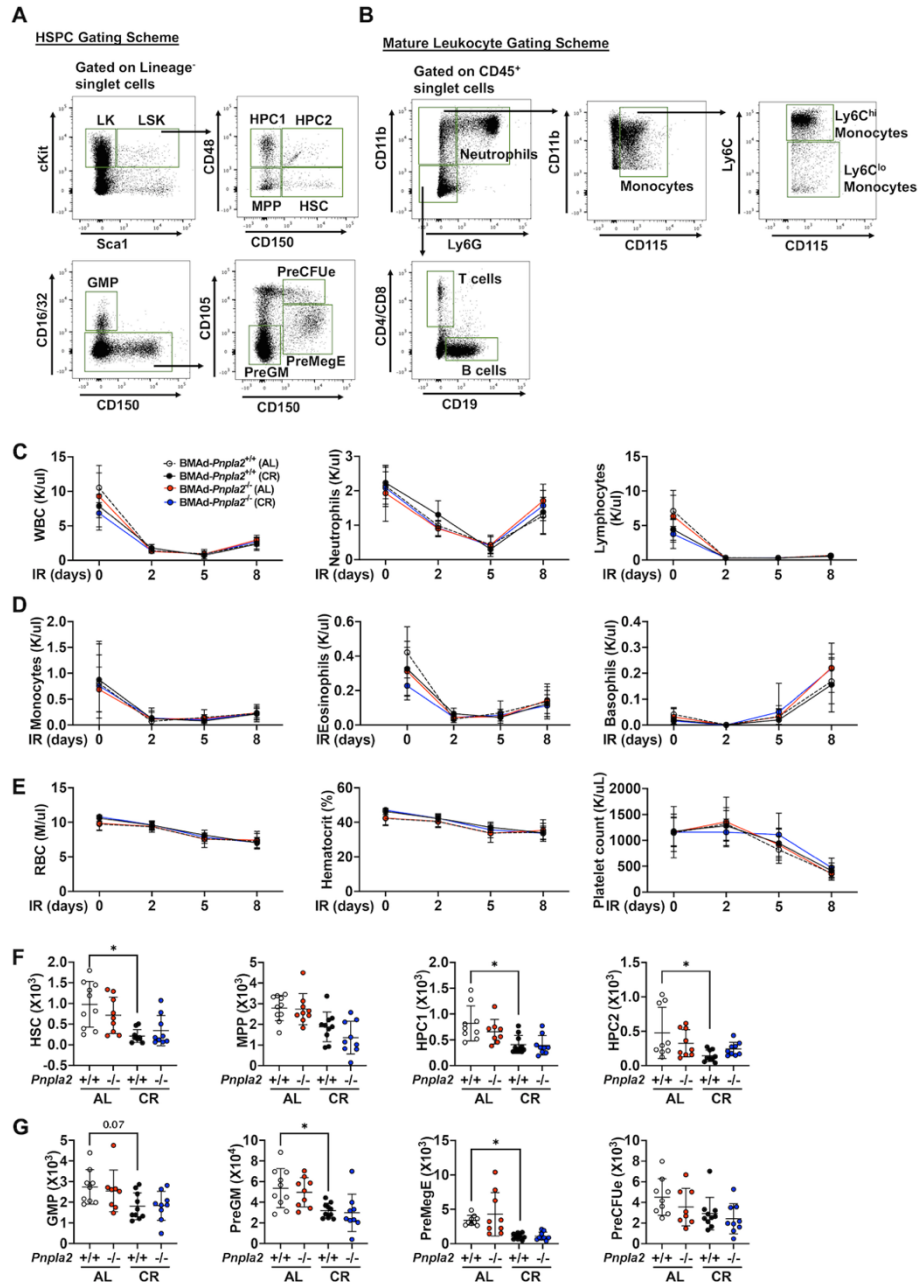


Figure 4 - figure supplement 1. Flow cytometry strategies for hematopoietic cells and sublethal irradiation-induced hematopoietic regeneration in *BMAd-Pnpla2^{-/-}* mice.

A-B. Hematopoietic cell gating strategies in hematopoietic stem/progenitor cells (HSPC, A) and mature leukocytes (B).

C-G. *BMAd-Pnpla2^{-/-}* mice and littermate controls (*Pnpla2^{+/+}*) underwent 30% caloric restriction (CR) for 20 weeks or remained on *ad libitum* (AL) diet, and then received a whole-body irradiation (6 Gy). Tail vein blood (~50 μ l) was collected every 2-3 days to monitor hematopoietic cell recovery. Mice were euthanized at day 9 post irradiation.

C-E. Data from complete blood cell counts shows dynamic changes of white- and red blood cells before and after irradiation.

F-G. Hematopoietic cells from two femurs were stained with cell markers to identify hematopoietic stem and progenitor cells.

Data are expressed as mean \pm SD. * indicates $P < 0.05$ with one-way ANOVA with Tukey's multiple comparisons test.

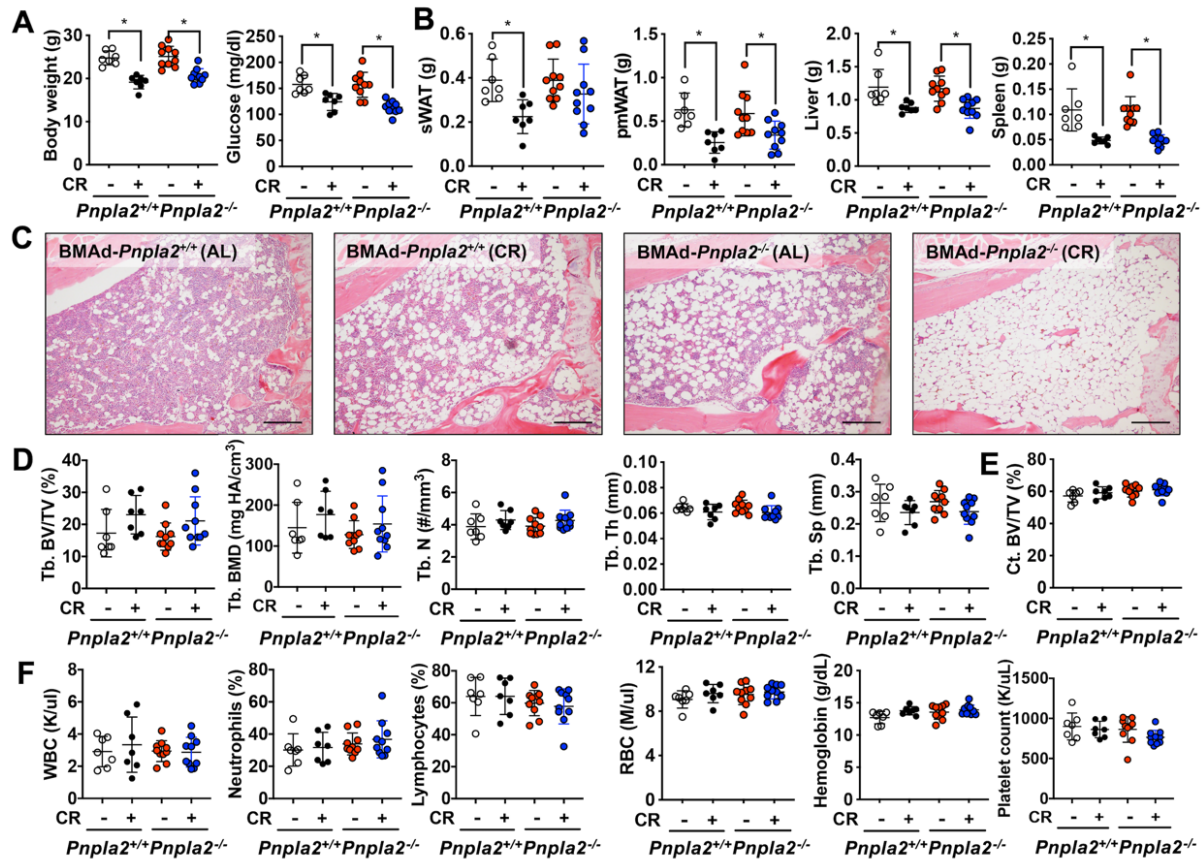


Figure 3 - figure supplement 3. BMAAd lipolysis is not required in female mice to maintain bone homeostasis under CR conditions.

BMAAd- $Pnpla2^{-/-}$ female mice and their wildtype controls ($Pnpla2^{+/+}$) at 18 weeks of age were fed *ad libitum* (AL) or underwent a 30% CR for another 6 weeks.

A-B. Final body weight and random glucose levels were measured (A). sWAT, parametrial WAT (pmWAT), liver and spleen weights were recorded during dissection (B).

C. Representative images from proximal tibiae were collected from decalcified and paraffin-sectioned bones. Scale bar, 200 μ m.

D-E. Trabecular and cortical bone variables were determined by μ CT analysis.

F. Complete blood counts (CBC) were performed to measure white- and red- blood cells in circulation.

Data are expressed as mean \pm SD. * indicates $P < 0.05$ with one-way ANOVA with Tukey's multiple comparisons test.

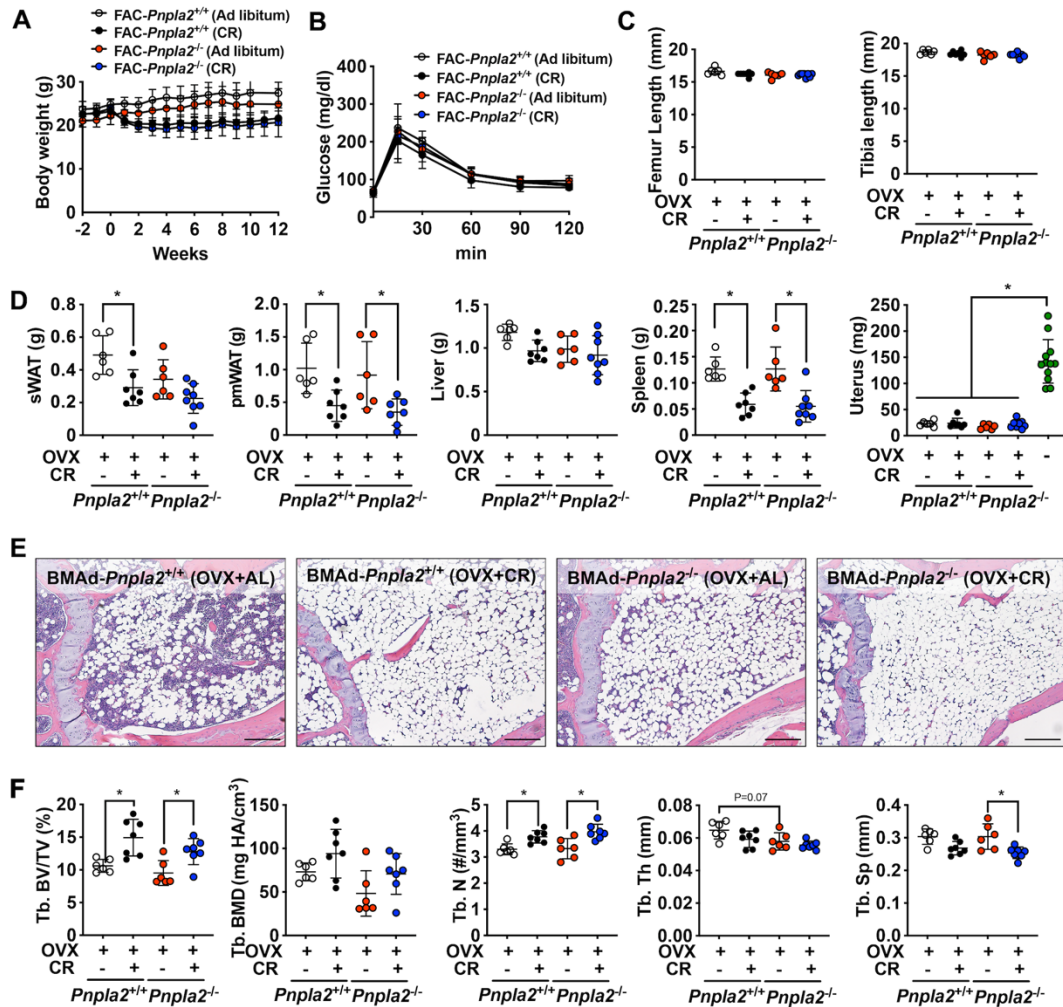


Figure 3 - figure supplement 4. BMAAd-lipolysis impairment in estrogen-deficient female mice does not affect CR-induced bone changes.

16 weeks old female mice underwent ovariectomy and recovered for 2 weeks, which were followed by 30% CR for 12 weeks. Changes in body weight (A) and glucose tolerance test (B) were recorded. Femoral and tibial lengths were measured (C). Weights of sWAT, pmWAT, liver, spleen, and uterus (green dots indicate sham mice) were measured during dissection (D). Trabecular bone parameters were determined by μ CT (E). Tb.: trabecular bone; BV/TV: bone volume fraction; BMD: bone mineral density; N: number; Th: thickness; Sp: separation. Data are expressed as mean \pm SD. * indicates $P < 0.05$ with one-way ANOVA with Tukey's multiple comparisons test.

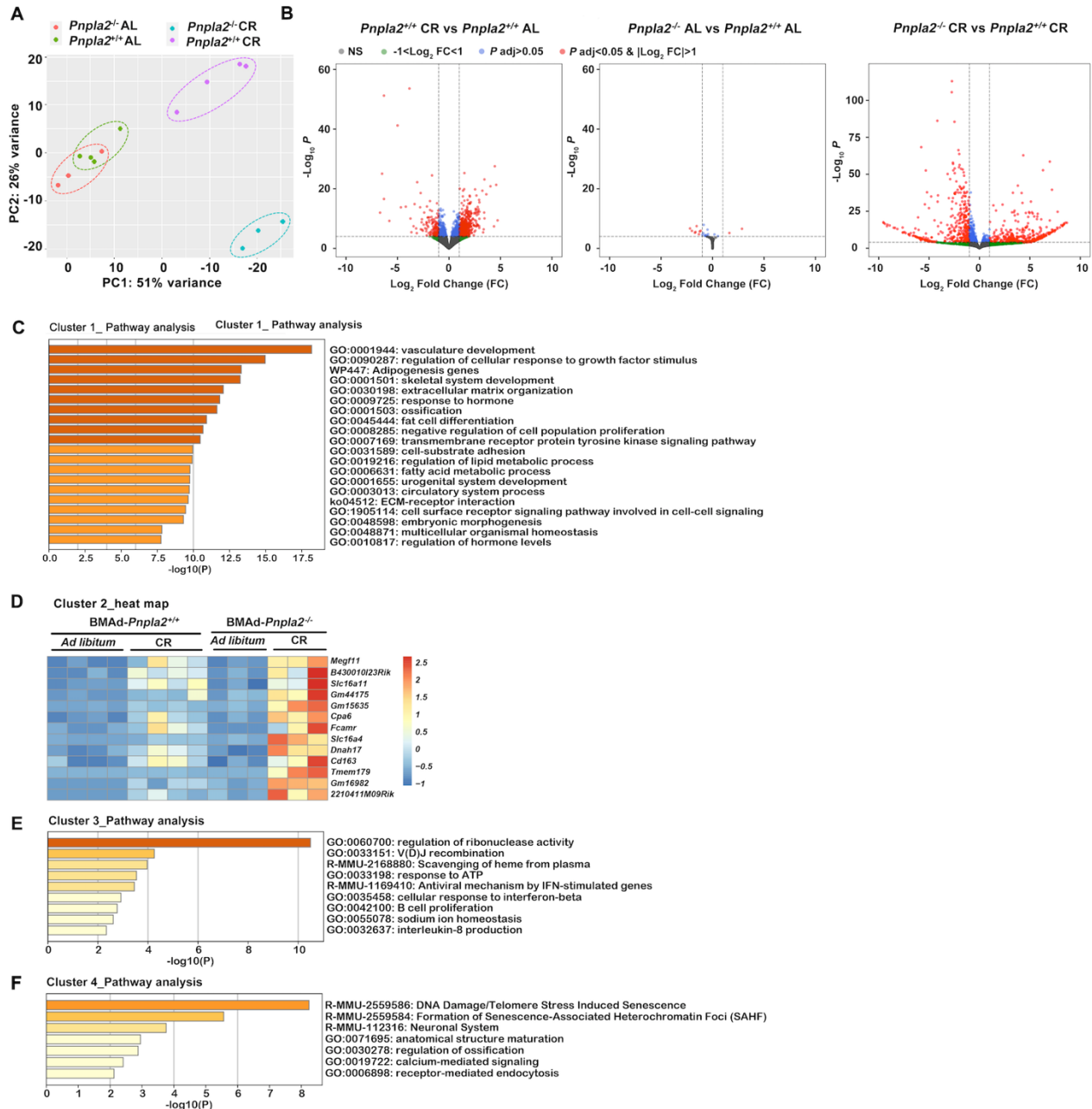


Figure 5 - figure supplement 1. CR causes profound changes in BMAT transcriptome.

24 weeks old male mice underwent 30% CR for 6 weeks. Distal tibial cBMAT was flushed and cBMAT from two mice were pooled as one sample for RNA sample preparation. High-quality RNA samples were submitted for RNAseq analyses.

A. Principal component analysis (PCA) plot shows the distinct transcriptional characters in CR groups with (purple dots) or without (aqua dots) *Pnpla2* in BMADs.

B. Volcano plots show the differential genes with $P \text{ adj} < 0.05$ & $|\text{Log}_2 \text{ fold change}| > 1$ in comparisons between BMAAd-*Pnpla2*^{+/+} CR versus AL (left), BMAAd-*Pnpla2*^{-/-} versus BMAAd-*Pnpla2*^{+/+} at AL (middle) and BMAAd-*Pnpla2*^{-/-} versus BMAAd-*Pnpla2*^{+/+} at CR (right).

C-F. Differential genes from comparison between BMAAd-*Pnpla2*^{+/+} CR versus AL were grouped into 4 clusters according to the alteration patterns. Pathway analyses were performed on each cluster except cluster 2, which gene set was not enriched in any pathways.

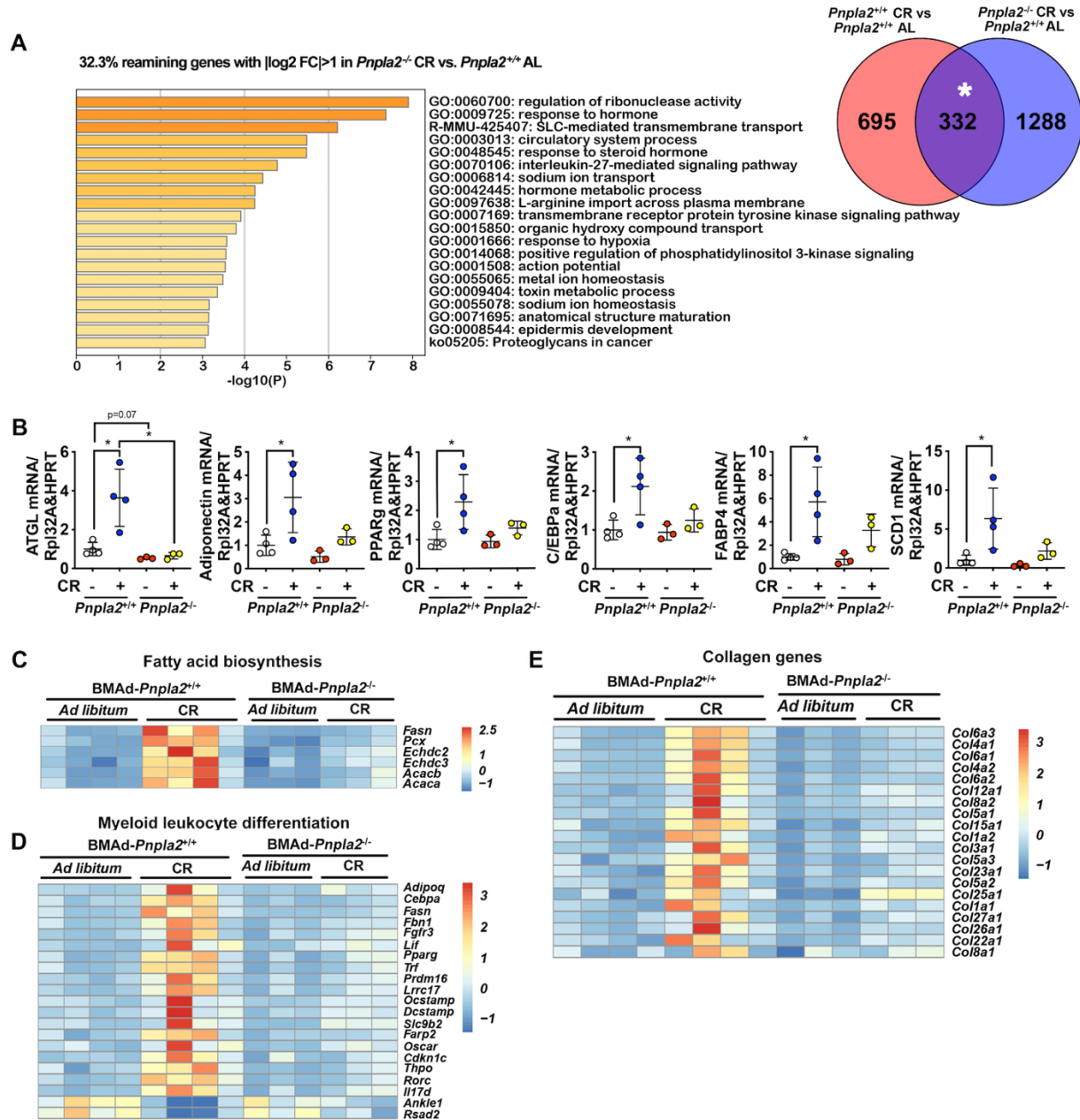


Figure 5 - figure supplement 2. BMAAd-*Pnpla2* deficiency causes extensive alterations to the bone marrow transcriptome only when coupled with CR.

24 weeks old male mice underwent 30% CR for 6 weeks. Distal tibial cBMAT was flushed and cBMAT from two mice were pooled as one sample for RNA sample preparation. High-quality RNA samples were submitted for RNAseq analyses.

A. Pathway analysis of gene set that respond to CR independent of *Pnpla2* deficiency in BMADs, indicated by * area.

B. qPCRs were performed to confirm the changes of adipogenesis genes in BMAT. Data are expressed as mean \pm SD. * indicates $P < 0.05$ with one-way ANOVA with Tukey's multiple comparisons test.

C-D. Heat maps for genes related to fatty acid biosynthesis and myeloid leukocyte differentiation.

E. Collagen genes that upregulated by CR in BMAAd-*Pnpla2*^{+/+} mice.